FEDERAL UNIVERSITY OF MATO GROSSO DO SUL
ENGINEERING, URBANISM AND ARCHITECTURE AND GEOGRAPHY FACULTY
ENVIRONMENTAL TECHNOLOGIES POST-GRADUATION PROGRAM

MANOEL LUCAS MACHADO XAVIER

Strategies for Urban Stormwater Wetlands

Campo Grande, MS

2018

FEDERAL UNIVERSITY OF MATO GROSSO DO SUL
ENGINEERING, URBANISM AND ARCHITECTURE AND GEOGRAPHY FACULTY
ENVIRONMENTAL TECHNOLOGIES POST-GRADUATION PROGRAM

MANOEL LUCAS MACHADO XAVIER

Strategies for Urban Stormwater Wetlands

Thesis presented as a partial fullfilment of the requirements for the degree of Doctor in the Environmental Technologies Post-Graduation Program of the Federal University of Mato Grosso do Sul in the Enviromental Sanitation and Hydraulic Resources area.

ADVISORS: **Prof. Dr. Johannes Gérson Janzen**

Prof. Dr. Heidi Nepf

Thesis Defence Committee:

Robert Schiaveto De Souza
Federal University of Mato Grosso do Sul

Fernando Jorge Corrêa Magalhães Filho
Dom Bosco Catholic University

Jhonatan Silva
Uniderp

Paulo Tarso Oliveira
Federal University of Mato Grosso do Sul

Campo Grande, MS

2018

Machado Xavier, Manoel Lucas
Strategies for Urban Stormwater Wetlands – Campo Grande, MS, 2018.

Thesis (Doctorate) – Federal Universtity of Mato Grosso do Sul, 2018.
Advisors: Prof. Dr. Johannes Gérson Janzen and Heidi Nepf

SUMMARY

DEDICATION

To Doreis, Fernanda and Zoraide. For everything.

ACKNOWLEDGEMENTS

To Professor Johannes, a friend and a guide since graduation days, thank you for the confidence, time, and knowledge provided throughout my journey.

To Professor Heidi, to be in the presence of your friendship and knowledge have been both an honor and a humbling experience, so thank you.

To my friend Paulo Henrique, a source of laughter, knowledge and help since graduation days.

To my brothers Carlos Leonardo and Paulo Leandro, who have always deposited immense trust in my choices and my work.

To my sisters in law (Amanda, Gabriela and Marcela), new sisters that have come along the way and were always there to provide any assistance needed.

To Helena and Joao Carlos for the advices.

To my cousins Yanna and Juliano, for the kind words.

To all CFD lab collegues who make the working hours much more pleaseant.

To all Nepf lab members who welcomed me with open arms and provided any assistance needed during my time at MIT.

To the CAU members who provided me with a new perspective on how to approach engineering problens.

To the members of Loko's House, two times a week our passion for fighting games brings us together to share countless laughs.

To all my friends and family, who, in one way or another, contributed to the conclusion of this work.

To the thesis defence committee members for the time and knowledge given to improve this work.

To the Project and Studies Funder – FINEP, the Foundation for Support to the Development of Teaching, Science and Technology - FUNDECT, and the MIT Abdul Latif Jameel World Water and Food Security Lab for funding this research.

LIST OF FIGURES

LIST OF TABLES

THESIS OVERVIEW

Urban Stormwater is an increasing environmental problem for cities across the world. The toxic mix of nitrogen, phosphorus, pathogens, sediments, heavy metals, etc, found in stormwaters threatens the ecological function of water systems, impairing critical ecosystem services cities need such as: water quality, aquifer recharge, flood protection, soil conservation, urban heat island reduction, biodiversity, and others. Only in the United States, it impairs 60,441 miles of rivers, 767,156 acres of lakes and 16,896 square miles of bays and estuaries (U.S. EPA, 2017).

To minimize the impact of stormwater on ecological systems (and even enable possibilities for re-use) stormwater needs to be treated. Unfortunetly, the cost for upgrading the existing infrastructure would require huge financial investment. In 2013, the American Society of Civil Engineers estimated that American cities need $298 billion over the next 20 years for wastewater and stormwater management and capital investment (CWNS, 2008)). However, federal funding sources for water infrastructure are diminishing. The Environmental Protection Agency (EPA) faced a cut of $309.9 million for 2015, which will largely be achieved by a $581 million reduction in two key water infrastructure funds, the State Clean Water Revolving Fund and the Drinking Water Revolving Fund (Ambrosio, 2015; Bloomberg, 2014; White, 2015). On top of this, regulations are tightening around stormwater and CSOs. Cities will have to spend more money to upgrade their infrastructure to meet higher levels of improvement.

Climate change will aggravate the necessity for stormwater management since it will make storms of greater intensity more likely, posing greater flood risks (Walsh, 2014).

Given these challenges and limitations, cities have turned to green infrastructure, such as bioswales, green roofs, detention ponds and treatment wetlands to capture and treat stormwater. The reason for this is that green infrastructure often performs at a lower cost than traditional infrastructure, while providing ancillary ecological and social benefits (Connop *et al*, 2016; U.S. EPA, 2015; Lovell and Johston, 2009; Atkins, 2015; Rousseau *et al*, 2008; Moore and Hunt, 202; Moore and Hunt, 2013).

Among these green infrastructures constructed wetlands using rooted plants have been increasingly integrated into urban water treatment (Carleton *et al*, 2001; Crow *et al*, 2007; Kadlec and Wallace, 2009; Melbourne Water, 2002), because they are passive, have low-maintenance and are simple to operate (compared to the traditional treatment

systems), while they also enhance habitat and provide recreational and aesthetic value to the urban landscape (Knight *et al*, 2001; Lee and Li, 2009; Rousseau *et al*, 2008). This natural infrastructure is harder to implement for stormwater treatment however, because stormwater events are episodic, such that the water level in a stormwater pond varies drastically over time-scales of days and weeks, making it difficult for rooted vegetation to establish and survive (Ewing, 1996; Greenway and Poulson, 2007; Headley and Tanner, 2006). Floating treatment islands (FTI) have been recently introduced as an alternative for stormwater treatment, because the floating vegetation can tolerate the swings in water depth associated with stormwater ponds (Headley and Tanner 2012). FTIs consist of emergent vegetation grown hydroponically on a floating structure (usually a foam mat). The roots extend downward into the water, providing a substrate for biofilm growth. Because uptake by roots and the biofilm they support is the main process of nutrient removal, the overall treatment provided by a stormwater pond with FTIs depends on both the volumetric extent of the root zone, as well as the contact time between the root zone and the polluted water (Headley and Tanner 2012; Chang *et al*, 2012).

Also, to function best, the flow in stormwater ponds or wetlands should approach plug flow conditions, in which all of the water entering the systems remains for the nominal residence time. In real systems however, the ideal plug flow condition is rarely achieved, short-circuiting for example play an important role in the pond-FTI hydrodynamics.

This study encompasses 3 original papers that looked into two key aspescts of the pond-FTI interaction using the Computational Fluid Dynamics (CFD)Technique as well as experimental methods.

Chapter 1 (to be submitted) describes different manners of representing vegetation in a CFD environmental as well as their advantages and disadvantages.

Chapter 2 was published as Balderas *et al*, (2017) consisted in the analysis of 34 island topographies to be inserted in a stormwater pond, the islands varied in number, size, shape, and placement, as well as an open basin and a serpentine design. The topographies were analyzed from 4 perspectives: hydrodynamic efficiency, water quality, habitat diversity and cost. This study advanced the ecological basis for green infrastructure design by demonstrating the superior performance of several specific island clusters landscapes for improving both the hydraulic and ecologic function of detention ponds and treatment wetlands.

Chapter 3 was published as Machado Machado Xavier *et al* (2017), it consists of different arrangements of FTIs with the goal of analyzing the degree to which different geometries contribute to the performance of a stormwater pond by examining the flow pattern and mass uptake within the individual root zones, this was done by using Computational Fluid Dynamics (CFD). This study showcased the influence of one FTI on another one placed in series and in parallel of one another, as well as how high and low flow regions can affect the FTI performance.

CHAPTER 1: MODELAGEM DA VEGETAÇÃO AQUÁTICA EM ESTUDOS DE CFD

RESUMO

O objetivo deste trabalho é apresentar duas formas de representar conceitualmente ou fisicamente a presença da vegetação no meio aquático usando o método *Computational Fluid Dynamics* (CFD), a saber, meio poroso e elementos geométricos simplificados. Três estudos de caso foram utilizados para apresentar as vantagens e desvantagens das duas representações. Na etapa da geometria e da malha, a representação da vegetação como meio poroso é mais simples, prática e rápida, que a representação da vegetação como elementos geométricos simplificados. Na parte da modelagem das equações, a representação do meio poroso não consegue capturar os processos de mistura no interior da vegetação, enquanto que a representação como elementos geométricos simplificados consegue capturar esses processos.

ABSTRACT

The goal of this work is to represent two manners of conceptually or physically representing the presence of vegetation in an aquatic environment using Computational Fluid Dynamics (CFD): the porous media approach and the simplified geometric elements. Three case studies were used to showcase the advantages and disadvantages of both representations. At the geometry and meshing phase, the porous media approach is simpler, faster and more practical then the simplified geometric elements. During the equation modeling, the porous media representation is not able to capture the mixing processes in the inner areas of the vegetation as well as the simplified geometric elements method.

Palavras-chave: Vegetação Aquática; Computational Fluid Dynamics; Modelagem Numérica.

Keywords: Aquatic Vegetation; Computational Fluid Dynamics; Numerical Modeling.

1. INTRODUÇÃO

A vegetação aquática desempenha um papel fundamental no funcionamento e na manutenção de ambientes naturais, como sistemas fluviais, regiões costeiras e pântanos. Dentre as suas funções ecológicas, pode-se citar a capacidade em remover, reter e degradar nutrientes, compostos orgânicos e inorgânicos e materiais tóxicos, melhorando a qualidade da água; o suporte no abrigo de outros organismos, promovendo a criação de habitats e o desenvolvimento da cadeia alimentar; e a habilidade em amortecer o impacto de ondas e em aumentar a estabilidade de margens e encostas, protegendo o ambiente da erosão hídrica (Nepf, 2012). Estima-se que esses e outros serviços desempenhados pela vegetação aquática no mundo possuem o valor econômico de 10 trilhões de dólares por ano (Costanza *et al*., 1997).

As interações que ocorrem entre a vegetação e o escoamento, e que resultam nos serviços mencionados acima, são um dos objetos de estudo da Mecânica de Fluidos Ambiental (mais conhecida em inglês como *Environmental Fluid Mechanics*). Por serem dinâmicas e complexas, as interações podem ser estudadas sob diversas escalas e para diferentes fins. Na pequena escala de uma folha, estudos têm investigado como ocorrem os processos de transferência de massa, responsáveis pelo fluxo de nutrientes e gases (Abdelrhman, 2003; Kleeberg *et al.*, 2010; Nepf, 2012). Na escala intermediária, manchas de vegetação têm sido estudadas na compreensão da hidráulica de canais (Sukhodolov and Sukhodolova, 2005; Green, 2006), na retenção e disposição de sedimentos (Cotton *et al.*, 2006; Bouma *et al.*, 2007) e na evolução da vegetação (Temmerman *et al.*, 2007; Vandenbruwaene *et al.*, 2011; Kondziolka and Nepf, 2014; De Lima *et al.*, 2015). Em grandes escalas, como a de paisagens vegetadas, estudos têm investigado os efeitos da vegetação na morfologia de regiões alagadas (Larsen and Harvey, 2011) e de rios (Tal and Paola, 2007).

Além dos tradicionais estudos de campo e em laboratório, a abordagem numérica utilizando a Fluidodinâmica Computacional, também conhecida como *Computational Fluid Dynamics* (CFD), tem se mostrado um campo promissor na área de escoamentos vegetados. O CFD é uma técnica capaz de representar, conceitualmente ou fisicamente, as interações vegetação-escoamento (Wilson *et al.*, 2005), e estudos recentes têm sido publicados nesta área (Stoesser *et al.*, 2010; Marjoribanks *et al.*, 2014; De Lima *et al.*, 2015; Chang and Constantinescu, 2015; Machado Xavier *et al.*, 2018). Dependendo do custo computacional e do nível de

detalhamento desejado, a vegetação pode ser representada de forma mais simples, como um coeficiente de rugosidade (Golzar, 2015), ou de forma detalhada, com seus galhos, ramos e folhas (Boothroyd *et al.*, 2016). Neste artigo são apresentadas duas formas de se representar a vegetação em modelos CFD, suas vantagens e deficiências, e como elas foram aplicadas em estudos de caso.

2. VEGETAÇÃO COMO MEIO POROSO

Uma das formas de representar a vegetação em CFD é pelo meio poroso, no qual a resistência oferecida pela vegetação ao escoamento é considerada no termo fonte das equações discretizadas de Navier-Stokes resolvidas pela modelagem CFD:

$$\frac{\partial u_j u_i}{\partial x_j} = -\frac{1}{\rho}\frac{\partial p}{\partial x_i} + \nu\frac{\partial^2 u_i}{\partial x_j \partial x_j} - \frac{\partial \overline{u_i' u_j'}}{\partial x_j} + S_{M,i} \quad (1)$$

onde i ou j = 1, 2 ou 3; x_1, x_2 e x_3 denotam as direções longitudinal (x), transversal (y) e vertical (z), respectivamente; u_1, u_2 e u_3 são as componentes correspondentes da velocidade média (i.e., $u_1 = u$, $u_2 = v$, e $u_3 = w$); $\overline{u_i' u_j'}$ é a componente das tensões de Reynolds, onde u' denota a parte flutuante da velocidade; p é a pressão; ρ é a massa específica do fluido; e $S_{M,i}$ é o termo fonte ou sumidouro. Para o presente caso há somente um sumidouro de quantidade de movimento o qual é tipicamente igual a:

$$S_{M,i} = \frac{\mu}{K_{perm}} v_i \quad (2)$$

onde K_{perm} é a permeabilidade (m^2), μ é a viscosidade dinâmica ($kg.m^{-1}s^{-1}$) e u_i é a velocidade ($m.s^{-1}$). O termo sumidouro cria uma perda de pressão no meio poroso que é proporcional à velocidade. A permeabilidade K_{perm} precisa ser calibrada para cada tipo de vegetação.

O desenho da vegetação como meio poroso é extremamente simples, prático e rápido, uma vez que a morfologia da vegetação (raízes, caules e folhas) não é levada em consideração e a forma geométrica do meio poroso é igual à da própria mancha de vegetação. Consequentemente,

o processo de geração da malha também é simples, prático e rápido, possibilitando facilmente o uso de geradores automáticos de malhas com boa qualidade (Yamasaki *et al.*, 2017).

Para ilustrar as vantagens e desvantagens de representar a vegetação como meio poroso e o seu passo a passo na modelagem CFD são apresentados a seguir dois estudos de caso. No primeiro estudo de caso foram utilizadas as medições de velocidade e de turbulência realizada por Downing-Kunz & Stacey (2012) num canal retangular com macrófitas flutuando na superfície. O modelo computacional possui 12,62 m de comprimento, 0,6 m de largura e 0,3 m de altura. A vegetação possui 0,62 m de comprimento, 0,58 m de largura e 0,125 m de altura, sendo representada por um domínio poroso (Figura 1).

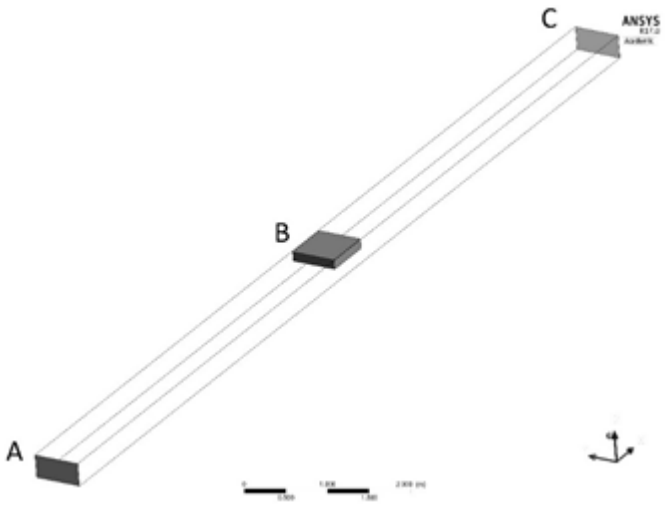

Figura 1: Geometria usada para o modelo computacional visando reproduzir os experimentos de Downing-Kunz and Stacey (2012). A representa a entrada, C representa a saída e B representa a vegetação.

Na entrada, o escoamento foi considerado uniforme com velocidade constante e igual a 5.5 $cm.s^{-1}$. Na saída, a pressão estática foi definida como sendo 0 Pa. Nas paredes, foi aplicada a condição de não deslizamento. Finalmente, na superfície livre foi aplicada a condição de simetria, com gradiente zero para as variáveis normais à superfície. O valor de K_{perm} foi variado entre 10^{-20} m^2 e 10^{-4} m^2 para ajustar os dados computacionais aos dados experimentais. A porosidade, razão entre o volume de vazios e o volume total, foi de 95%.

A Figura 2 apresenta os perfis de velocidade vertical para três permeabilidades. Os perfis de velocidade foram extraídos para a linha vertical que passa por 70% do comprimento da zona porosa. O melhor ajuste foi obtido para $K_{perm} = 10^{-6}$ m^2. Note que apesar de existir um

distanciamento entre valores experimentais e computacionais no seio do escoamento, o comportamento da velocidade ao longo da profundidade é bem descrito, havendo um bom ajuste no fundo do canal e junto ao e no interior da vegetação.

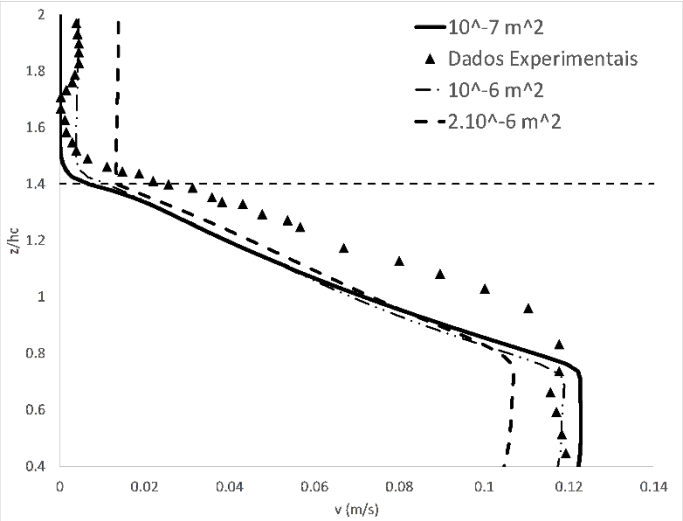

Figura 2: Comparação entre os dados experimentais e computacionais. z é a distância vertical, hc é a espessura da zona porosa, e u é a velocidade na direção do escoamento. A linha tracejada indica o fundo da zona porosa.

O segundo estudo de caso consiste na simulação do escoamento em um canal vegetado que possui um grupo de manchas de vegetação emergente (não submersas). No domínio computacional, o canal retangular apresenta 25,3 m de comprimento e 4,4 m de largura, e cada mancha circular de vegetação possui diâmetro igual a 22 cm (Figura 3a). As 54 manchas foram aleatoriamente inseridas no canal, mantendo-se uma distância de 3,08 m da entrada e 6,82 m da saída. O escoamento chega no canal a uma velocidade de entrada, U_0, igual a 9,5 $cm.s^{-1}$. Considerando que a vegetação é emergente, os principais efeitos das interações com o escoamento ocorrem no plano horizontal, e, portanto, o modelo pode ser representado em 2-D, assumindo profundidade unitária (De Lima *et al.*, 2015).

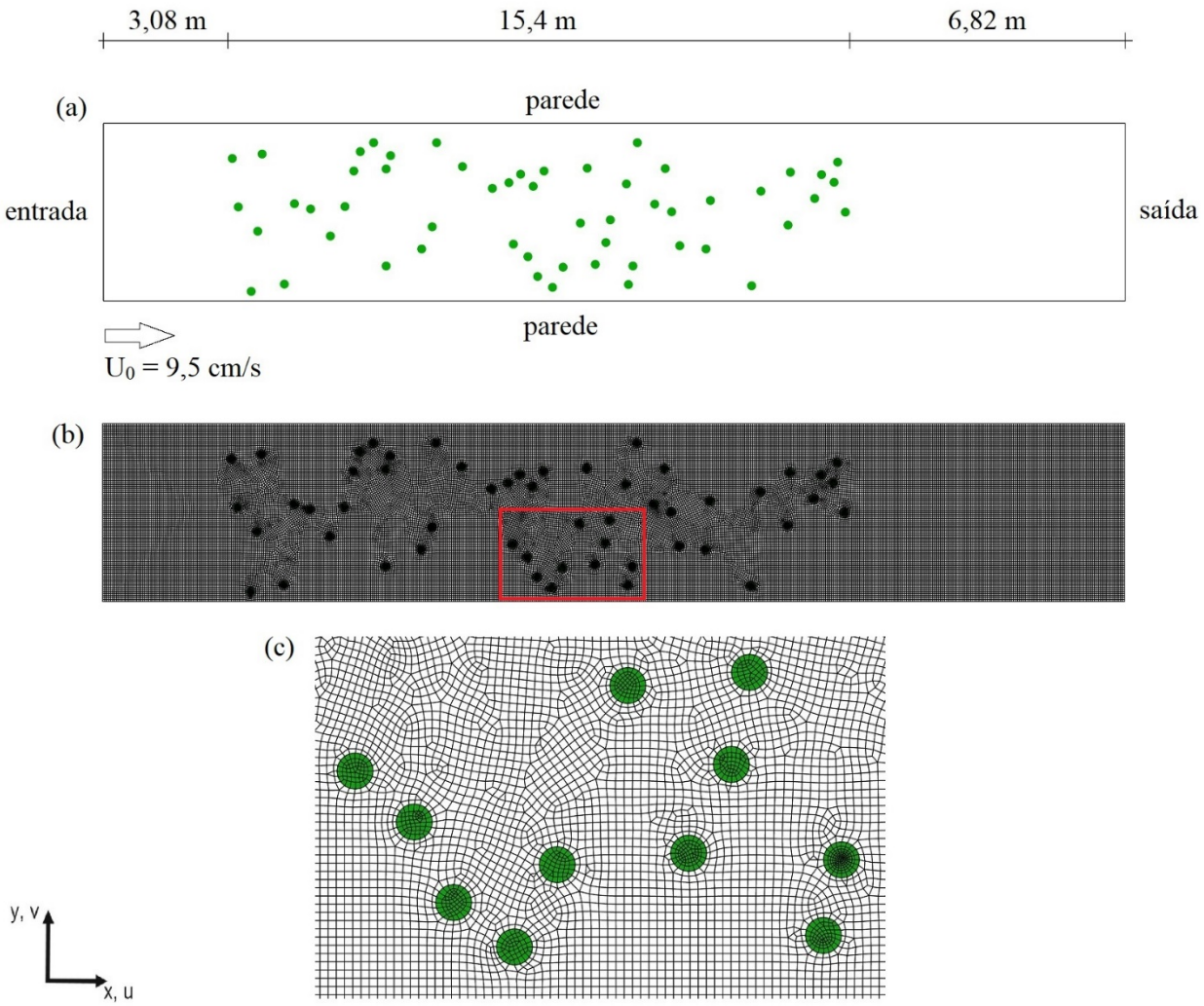

Figura 3: (a) Geometria e (b) malha típica de um canal com 54 manchas de vegetação emergente representadas como meio poroso, em vista superior. Em (c), detalhe da malha dentro e ao redor das manchas de vegetação.

Assim como no primeiro estudo de caso, a malha foi gerada de forma automática (Figura 3b). Os volumes de controle ficaram menores nas regiões de alto gradiente de velocidade, como na interface entre a vegetação e a água (Figura 3c). A permeabilidade do meio poroso foi calibrada com dados experimentais de Zong e Nepf (2012), obtendo-se o melhor ajuste para K_{per} = 1/70000 m^2 (Figura 4).

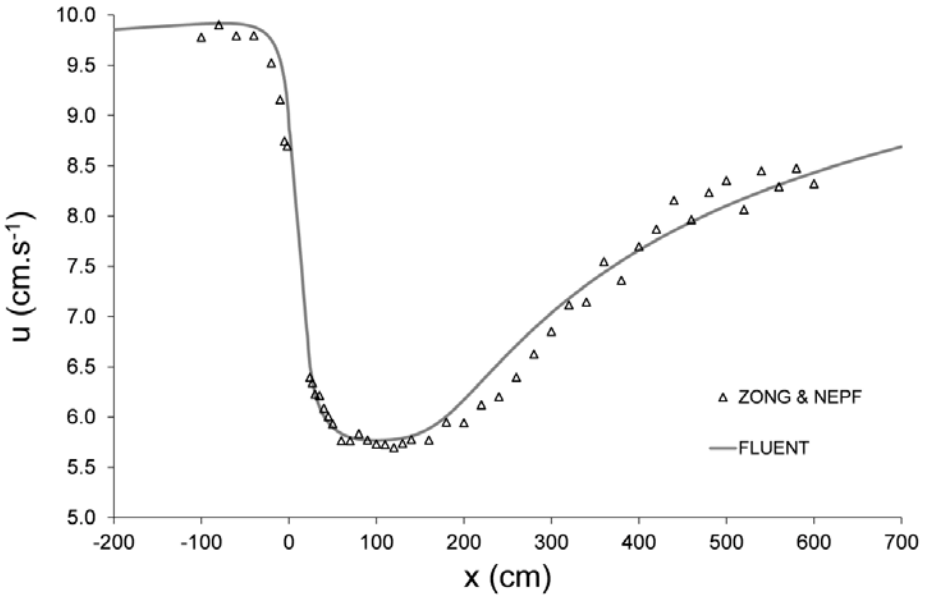

Figura 4: curva de calibração da permeabilidade para uma mancha de vegetação. Os dados mostram a velocidade u na linha de centro da mancha. O erro máximo entre os dados numéricos e os experimentais foi de 6%.

A Figura 5 mostra o campo resultante de velocidade no canal após a simulação. O padrão inicial do escoamento foi modificado pelas manchas, originando regiões de velocidade reduzida (menor que U_0) na esteira das manchas, e regiões de alta velocidade (maior que U_0) nas laterais das manchas (Zong and Nepf, 2012). Há também o efeito das interações entre as manchas, também conhecidas como *feedbacks*, sobre o escoamento (De LIma *et al.*, 2015).

Além da hidrodinâmica de grande escala que ocorre ao redor da mancha de vegetação, e cuja representação pode ser obtida através do modelo poroso, é importante destacar que as manchas de vegetação também produzem uma hidrodinâmica de pequena escala (na escala de caules no interior da mancha) que induzem processos de mistura transversal e longitudinal (Tsavdaris *et al.*, 2013). Dentre os processos de mistura transversal, destacam-se a difusão turbulenta e a dispersão mecânica (Nepf, 1999), enquanto que, dentre os processos longitudinais, destacam-se o aprisionamento de vórtices e a dispersão da esteira secundária (cisalhamento diferencial) ao redor dos "cilindros" da vegetação (raízes e caules) (White and Nepf, 2003). Neste caso, o modelo poroso não é capaz de capturar a hidrodinâmica de pequena escala.

Para melhor representar a vegetação, estudos têm configurado a zona porosa com parâmetros que levem em consideração a turbulência adicional causada pelos "cilindros" (Sonnenwald *et al.*, 2017). Os resultados iniciais são promissores, sendo aparentemente possível estimar valores adequados para cada tipo de vegetação. Portanto, espera-se que no futuro próximo

seja possível modelar os efeitos da turbulência utilizando o meio poroso.

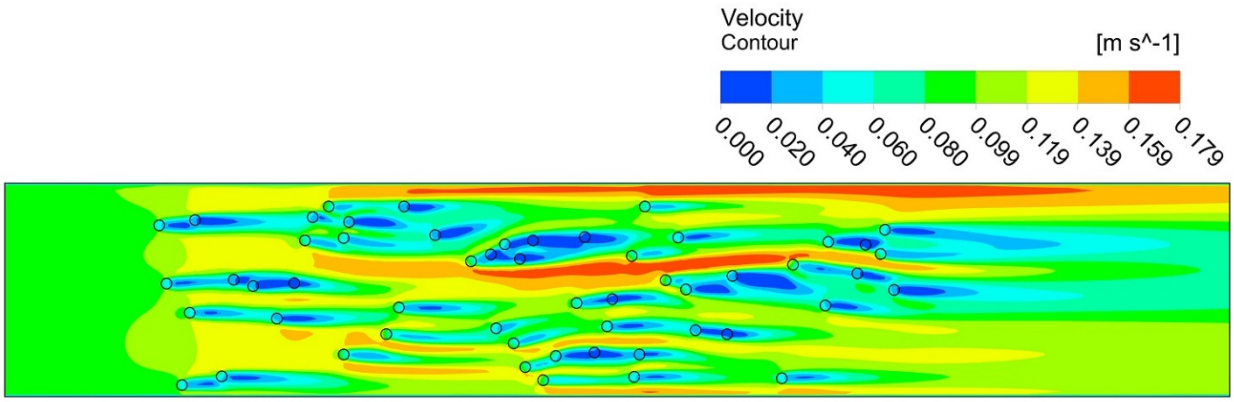

Figura 5: Campo de velocidades no canal vegetado. As 54 manchas circulares de vegetação foram representadas como meios porosos.

3. VEGETAÇÃO COMO ELEMENTOS GEOMÉTRICOS SIMPLIFICADOS

A segunda forma de representar a vegetação é desenhar a vegetação com todos os seus detalhes ou de forma simplificada. Ainda que existam pesquisadores argumentando no sentido de desenhar todos os detalhes da vegetação (por exemplo, Boothroyd *et al.*, 2016 defenderam o desenho dos detalhes para um ramo de vegetação), a geometria se torna tão trabalhosa que se torna inviável utilizar esta aproximação para situações reais de manchas de vegetação. A maioria dos pesquisadores tem desenhado simplificadamente a vegetação na forma de cilindros rígidos ou flexíveis, com os cilindros possuindo a mesma altura da vegetação real e com a fração de volume sólido da representação da vegetação igual à da própria vegetação. Entretanto, o principal parâmetro que deve ser garantido como igual no desenho simplificado da vegetação e no modelo real deve ser a área frontal da vegetação por volume. Muito embora seja esperado que a distribuição dos cilindros que compõe a vegetação real seja aleatória, testes preliminares mostraram que não existe diferença significativa entre utilizar um arranjo regular de cilindros ou distribui-los de forma aleatória.

No caso da representação por elementos simplificados, a perda da quantidade de movimento na vegetação ocorre devido a força de arrasto que ocorre nos cilindros. Usualmente são utilizados modelos de turbulência que permitem reproduzir bem o escoamento médio e turbulento, apesar de não predizerem bem os detalhes quantitativos da turbulência, a saber, escalas de cisalhamento e esteira (Defina and Bixio, 2005). Eventualmente o coeficiente de

arrasto precisa ser calibrado. Em poucas situações são empregados modelos mais robustos (e.g. *Large Eddy Simulation*), permitindo a obtenção quantitativa da turbulência (Stoesser *et al.*, 2009).

Para ilustrar o uso da representação por elementos simplificados na modelagem CFD de escoamentos com vegetação, foi utilizado o problema de Zong & Nepf (2012), constituído de um canal de 10 m de comprimento e 1,2 m de largura (Figura 6a). Neste caso, o problema foi considerado bidimensional, isto é, com profundidade unitária. A velocidade de entrada no canal, U_0, foi de 9,5 cm.s^{-1}. Uma mancha de vegetação circular com diâmetro D = 22 cm foi inserida 3

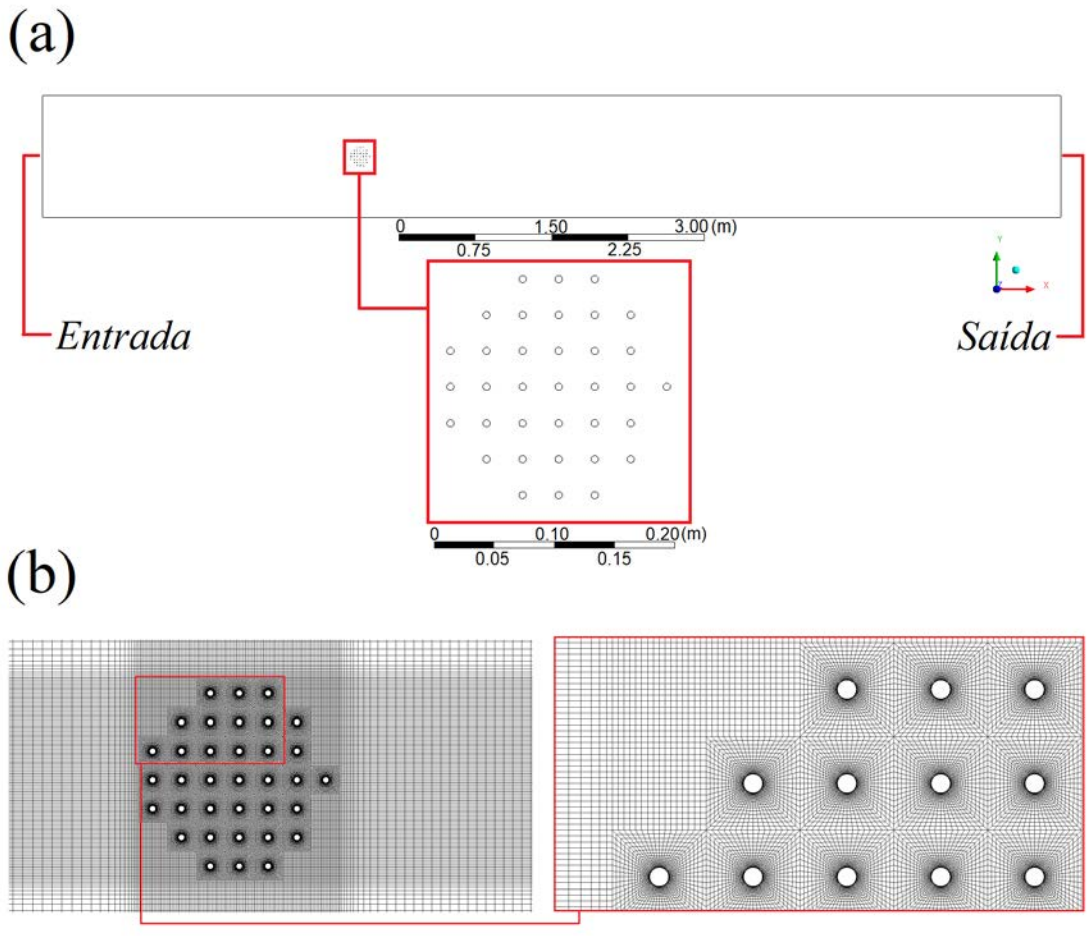

Figura 6:(a) Geometria do canal com uma mancha de vegetação e (b) Detalhamento da malha ao redor e no interior de uma mancha de vegetação emergente representada como elemento geométrico simplificado.

Para simplificar a malha computacional, os cilindros foram arranjados em um formato quadrado, ao invés do formato circular usado por Zong & Nepf (2012). A justificativa para tal procedimento está nos resultados experimentais obtidos por Vandenbruwaene *et al.* (2011), que

encontraram escoamentos similares próximo manchas de vegetação circulares ou quadradas com mesma densidade de cilindros. A mancha computacional possui 35 cilindros rígidos com diâmetro de 0,6 cm, produzindo uma fração de volume sólido aproximadamente igual a 0,03. A área frontal por unidade de volume foi 0,06 cm^{-1}. Note que desenhar uma mancha de vegetação com elementos geométricos ainda que simplificados já é bem mais complexo que desenhar a mesma mancha considerando meio poroso.

Como no caso da representação com elementos geométricos se deseja obter informação do escoamento e da turbulência no interior da mancha, é preciso existir uma malha refinada ao redor de cada um dos cilindros (Figura 6b). Uma das possibilidades é gerar uma estrutura de malha do tipo O-grid ao redor de cada cilindro. Para construir a estrutura O-grid utiliza-se geradores semiautomáticos que trabalhem a estruturação em blocos. Esses geradores de malha, quando comparados com os automáticos, consomem muito mais tempo para se conseguir a malha ideal.

4. RESULTADOS E DISCUSSÃO

Os campos de velocidade (u, v) são os principais resultados a serem obtidos para estudos do escoamento ao redor de manchas de vegetação. Por que é a partir destes campos que será possível inferir as regiões mais provavéis para crescimento e desenvolvimento da vegetação presente no canal. Por isso é preciso garantir que a representação da vegetação nas simulações seja capaz de reproduzir, sobretudo, as mesmas caracteristícas e padrões destes campos de escoamento obtidos experimentalmente. Outras informações como a energia cinética turbulenta também podem ser importantes, no entanto, são quantidades mais dificies de se reproduzir com precisão uma vez que dependem da escolha dos modelos de turbulencia e até mesmo de uma calibração de suas constantes empíricas.

Alguns comprimentos característicos determinam como será o padrão dos campos de escoamento devido a presença da vegetação, tais como: L_0 que é a distancia a montante da mancha onde o escoamento inicialmente é afetado pela vegetação e; L_1 que é a distancia a jusante da mancha onde a velocidade do escoamento é mais reduzida, denominada esteira estacionária. Estes

comprimentos são função do tamanho (diametro, D) e densidade da mancha (a) (Zong & Nepf, 2012).

A simulação de um canal com uma única mancha de vegetação (D = 22 cm, a = 0,13 cm^{-1}) mostrou que o campo de escoamento uniforme que se aproximava da vegetação começou a ser alterado a uma distancia $L_0 \approx 1.4D$ a montante da mancha, um resultado que é consistente com a ordem de grandeza apresentados experimentalmente por outros autores (Rominger & Nepf, 2011 e Zong & Nepf , 2012).

Quando o campo de escoamento atinge a vegetação, parte do escoamento é desviado e acelerado lateralmente e outra parte atravessa a mancha perdendo quantidade de movimento resultando em uma região com baixos valores de velocidade diretamente atrás da mancha (Figura 7). Chen et al. (2012) sugeriram a seguinte relação para a velocidade de saída da mancha, U_e:

$$\frac{U_e}{U_0} \approx 1 - 0.21 C_D a D \tag{3}$$

Onde $C_D aD$ é o coeficiente de bloqueio de fluxo devido ao arrasto proporcionado pelos cilindros que compõem o arranjo da mancha. A eq. (3) prediz $U_e/U_0 \approx 0.40$, para o bloqueio de fluxo da mancha modelada ($C_D aD$ = 2,86). Este valor é bem próximo do obtido pela simulação, que apresentou $U_e/U_0 = 0.6$. Não há regiões com velocidades negativas, a jusante da mancha, o que também está em acordo com Chen et al. (2012), que não observaram esse comportamento atrás de manchas com baixos bloqueios de fluxo ($C_D aD < 4$).

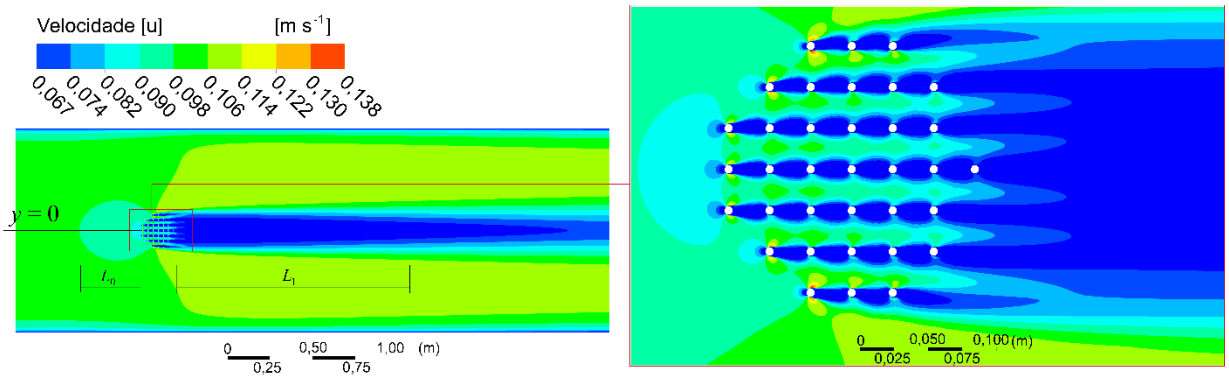

Figura 7:Campo de escoamento para um canal com uma única mancha de vegetação representada por um arranjo de cilindros (D = 22cm e a = 0,13 cm-1). A linha de centro y = 0 é a região na qual os dados são obtidos para comparação.

A extensão da esteira estacionária é determinada pelo valor L_1. Na posição $x = L_1$, e além deste ponto a velocidade começa a aumentar novamente até que a uma grande distancia a jusante da mancha o escoamento volte a se tornar completamente desenvolvido. Considerando que existe depêndencia da velocidade no interior da esteira estacionária ($0 < x < L_1$) com o bloqueio de fluxo, Chen et al. (2012) propuseram a seguinte equação para predizer o comprimento L_1 da esteira, para manchas com baixo bloqueio de fluxo ($C_D aD < 4$):

$$\frac{L_1}{D} = 2.5\left[\frac{8-C_D aD}{C_D aD}\right] \quad (4)$$

A eq. (4) prediz $L_1/D \approx 4{,}5$. Que está em boa concordancia com a simulação, que apresentou $L_1/D = 4{,}1$.

Mais especificamente foi possível obter também os valores das componentes u e v da velocidade e a energia cinética turbulenta, k (Figura 8). O valores apresentados foram obtidos na linha de centro do canal ($y = 0$) que é a mesmo lugar onde essas grandezas foram obtidas experimentalmente por Zong & Nepf (2012).

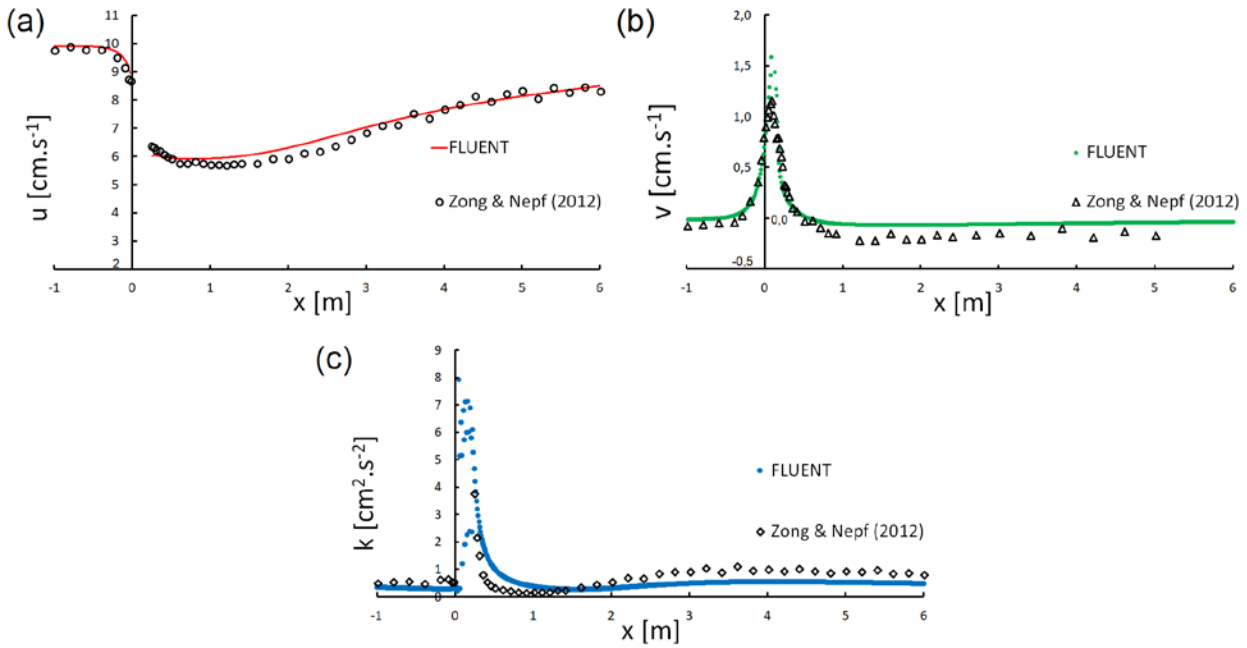

Figura 8: Comparação entre resultados experimentais de Zong & Nepf ap longo da linha de centro da mancha (2012) e computacionais. (a) Velocidade média longitudinal (u). (b) Velocidade média transversal (v) (c) Energia cinética turbulenta (k).

5. CONCLUSÃO

Este artigo apresentou dois métodos que têm sido utilizados para representar a vegetação aquática em modelagens CFD, e que visam compreender a influência da vegetação no escoamento. Três estudos de caso foram apresentados, os quais confirmam a complexidade da interação escoamento-vegetação e tornam claro os avanços necessários nesta área da Mecânica dos Fluidos e Hidráulica. Na parte da geometria e da malha, a representação da vegetação como meio poroso é mais simples, prática e rápida do que a representação da vegetação como elementos geométricos simplificados. Na parte da modelagem das equações, a representação pelo meio poroso não consegue capturar os processos de mistura no interior da vegetação, ainda que avanços recentes têm possibilitado resolver parte do problema. Por sua vez, a representação por elementos geométricos simplificados consegue capturar os processos de mistura no interior da vegetação. O detalhamento desta informação depende do modelo de turbulência utilizado.

CHAPTER 2: ISLAND TOPOGRAPHIES TO REDUCE SHORT-CIRCUITING IN STORMWATER DETENTION PONDS AND TREATMENT WETLANDS

ABSTRACT

Urban stormwater is an increasing environmental problem for cities worldwide. Many cities have turned to green infrastructure solutions, which provide water treatment and retention while also harnessing other ecosystem services. This study considered the design of detention ponds and treatment wetlands with the goal of improving hydraulic performance (specifically reducing short-circuiting) while also increasing habitat diversity. Fifty-four basin topographies, including a variety of islands and berms, were compared to an open and a traditional serpentine basin. Using scaled physical models the hydraulic performance of each design was evaluated using tracer studies to construct the residence time distribution and to visually observe the circulation pattern. In addition, the earthwork construction cost and habitat diversity index (based on the Shannon-Weaver entropy measure) were estimated at field scale. The results reveal multiple design options that improve hydraulic performance, relative to both the open and serpentine basins, and which represent a range of habit diversity and cost. General guidelines for optimal configurations are discussed.

Keywords: Stormwater Detention Ponds, Treatment Wetlands, Residence Time, Green Infrastructure Design

6. INTRODUCTION

Urban stormwater is an increasing environmental problem for cities worldwide. In the United States today, stormwater impairs 60,441 miles of rivers, 767,156 acres of lakes, and 16,896 square miles of bays and estuaries (U.S. EPA, 2017). Urban stormwater is a growing source of water pollution, and the number of natural ecosystems impaired by stormwater continues to rise (U.S. EPA 2015). Cities depend on these ecosystems for critical services, such as climate regulation, noise reduction, air purification, and flood protection (Gómez-Baggethun et al. 2013). The latter is especially important given that climate change will bring storms of increasing

intensity, posing greater flood risks (Walsh 2014). To address this challenge, many cities have turned to green infrastructure, such as bioswales, green roofs, detention ponds, and treatment wetlands, to capture and treat stormwater. Green infrastructure often performs at a lower cost than traditional infrastructure, while providing ancillary ecological and social benefits (Connop et al. 2016; U.S. EPA 2015; Lovell and Johnston 2009; Atkins, Inc. 2015; Rousseau et al. 2008; Moore and Hunt 2012, 2013). This paper considers landscape designs for detention ponds and treatment wetlands that offer opportunities to provide new habitat and re-introduce nature into cities (Ghermandi and Fichtman 2015; Worrall et al. 1997; Connor and Luczak 2002).

Habitat heterogeneity supports biodiversity, which underlies the provision of ecosystem services (Elmqvist et al. 2013). Research on treatment wetlands has shown that heterogeneity in landscape is the key to creating habitat. The EPA recommends eschewing rectangular basins in favor of sinuous edges and using varied slopes and grades to create different water depths (U.S. EPA 2000), which is also echoed by Worrall et al. (1997). Other researchers have noted the contribution of topography in constructed wetlands to habitat diversity and species richness (Vivian-Smith 1997; Sleeper and Ficklin 2016). In mitigation wetlands, micro-topography has been shown to aid nitrogen cycling and removal (Wolf et al. 2011).

To function best, the flow in a detention pond or constructed wetland should approach plug flow conditions, in which all of the water entering the system remains for the nominal residence time,

$$T_n = V/Q, \tag{5}$$

with V the system volume and Q the inflow rate. However, in most situations, ideal flow is not achieved, and short-circuiting of flow between the inlet and outlet occurs. In shallow basins, short-circuiting is associated with asymmetric circulation patterns that grow from instabilities at the inflow (Dewals et al. 2008; Dufresne et al. 2010). In vegetated regions, short-circuiting may be promoted by heterogeneous distributions of vegetation or by channels cutting through vegetation (Dierberg et al. 2005; Lightbody et al. 2008). Short-circuiting undermines the performance of a pond or wetland by allowing much of the water to exit in less than T_n. Because many of the biochemical, filtering, and settling processes that reduce pollutant levels are first-order reactions, there is a greater dis-benefit to pollutant removal for parcels of water leaving before T_n

compared to the benefit of leaving after $T_{n,}$, so that short-circuiting diminishes overall pollutant removal.

Because of its adverse effects, engineers have devoted substantial research to identify geometries that reduce or eliminate short-circuiting. For example, short-circuiting is reduced in basin geometries with long aspect ratios (Thackston et al. 1987) or with sinuous channels or baffles (Savickis et al. 2016; Farjood et al. 2015). In treatment wetlands, the insertion of unvegetated deep zones perpendicular to the flow path has been shown to counter-act the short-circuiting associated with channels that cut through vegetated regions (Lightbody 2007). Other studies have suggested islands to deflect inflow and improve the circulation pattern within treatment wetlands and ponds (German and Kant, 1998). Persson tested 13 pond designs, including 2 with islands, using MIKE21, a depth-averaged numerical model. Persson found that the scenario with an island at the inlet reduced short-circuiting, compared to a basin with no island or with berms (Persson et al. 1999, Persson 2000). In 2004, Adamsson and colleagues physically modeled a square island in front of the inlet, considering islands with edges parallel and rotated 45 degrees to the basin edges. The addition of the island decreased short-circuiting, with the greater benefit from the parallel island than the rotated island (Adamsson et al. 2002). In contrast, Khan et al. (2011) found that the addition of an island (either parallel or rotated) increased short-circuiting and decreased the performance of a scaled detention pond model. Khan attributed the poor performance to the sloping walls of the narrow basin, which created shallow regions through which the inflow jet skirted around the island. The Khan and Adamsson studies together suggest that the potential impact of a deflector island is sensitive to the size of the island, the position within the basin and the basin geometry. Therefore, while some promising results have been reported for islands, additional studies are needed to identify the optimum island designs. This paper expands on previous research by exploring more complex island topographies, along with open basin and serpentine designs for comparison. Each design was evaluated for hydraulic performance, habitat diversity, and earthwork construction cost.

7. EXPERIMENTAL METHODS

Experiments were conducted in two phases. In the first phase, a set of simple geometric shapes were cast in concrete and used to create 20 basic wetland configurations (Figure 9),

including berms, islands, and pinch points, which are constrictions that separate the basin into two sub basins. The results of phase 1 indicated that a cluster of islands near the inlet provided the greatest hydraulic improvement, so that phase two of the experiments focused only on islands, constructed with greater topographic detail. Specifically, phase 2 included 34 designs, exploring different number, size, shape, and placement of islands (Fig. 2). In both testing phases, the hydraulic performance was evaluated using tracer studies to estimate the residence time distribution and associated metrics (Section 2.2). In addition, the earthwork construction cost and habitat diversity were estimated for each of the topographies at field scale (Sections 2.3 and 2.4).

7.1. Physical Models

The first phase of experiments used a scaled model of the detention basin described in Khan et al. (2013), designed with the Froude number scaling detailed in Shilton (2001). The model basin measured 120 cm by 40 cm and had sloped sides, with a 1-cm inlet and outlet centered 1 cm above the bed. The water depth was $H = 3.0 \pm 0.1$ cm, which was sufficient to avoid surface tension affects (Shilton 2001). With a flow rate of Q = 4.8 x 10-5 m3/s, the nominal residence time for the open basin (which was considered the control, denoted with sub-script '*nc*') was $Tnc = 300 \pm 10$ s. Concrete shapes were placed inside the basin to create 20 basic configurations of berms, island clusters, and pinch points (Figure 9).

In the second phase, 34 island topographies were tested, including islands of different number, size, shape, and placement, as well as an open basin and a serpentine design (Figure 10). These topographies were designed in Rhinoceros, a 3D computer-aided design (CAD) program, and robotically milled out of high-density foam using a CNC machine. Each model measured 40.5 cm wide and 60 cm long. Relative to the full-scale prototype, the model height was exaggerated by a factor of two to avoid surface tension effects. For ease of fabrication, the islands were made with flat faces.

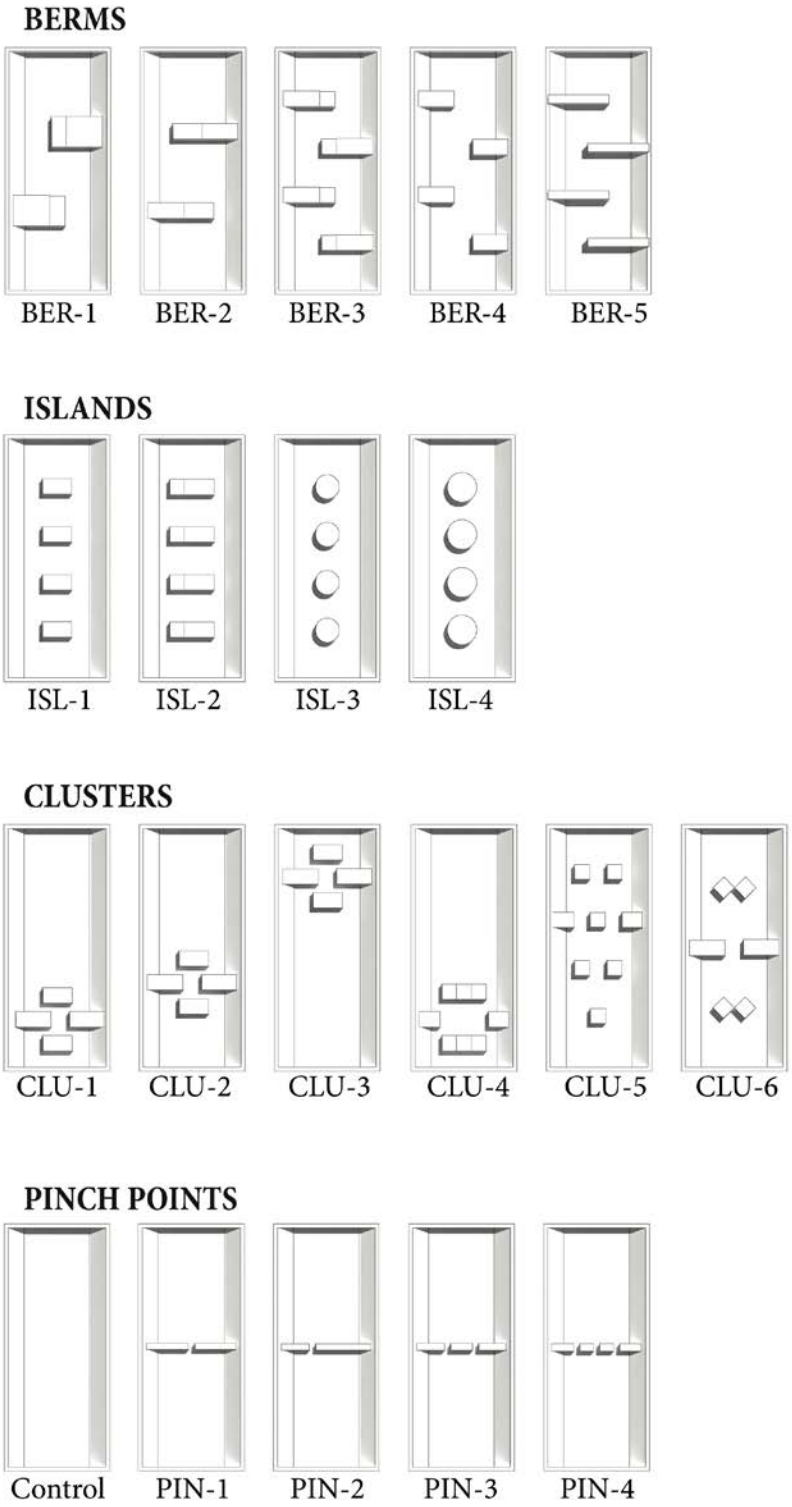

Figure 9: Top view of the phase 1 experimental basins, each 120 cm by 40 cm and with sloped sides. Flow is from bottom to top in each schematic.

Figure 10: Top view of phase 2 topographies, 40.5 cm wide and 60 cm long. Flow was from left to right.

The model topographies were placed in a plexiglass flume measuring 3.75 m long and B = 0.41 m wide (Figure 11). Downstream of each topography, a flat bed was added to create a test basin of length L = 93.0±0.2 cm. The topographies were attached to a concrete base to prevent floating. The flume was filled to a water depth of H= 3.3 ± 0.2 cm over the model. A variable speed pump provided a discharge of 0.200 ± 0.011 L s^{-1}. To produce a straight inflow, flow entered the test basin through a 28-cm long inlet channel with the same width as the basin inlet, 2.2 cm. The outlet was 3 cm wide to accommodate the fluorometer. The Reynolds number of the inflow was $Re = Uh/\nu$ = 9000, with U the inflow velocity and ν the kinematic viscosity. Consequently, the circulation pattern was inertia-dominated and should be representative of the flow field at full-scale. For the phase 2 experiments, the nominal residence time of the open basin, which was used as a control, was T_{nc} = 63 ± 3 s, (with subscript "c" denoting control). The uncertainty reflects the variation in flow rate. Two replicate experiments were conducted for each of the topographies.

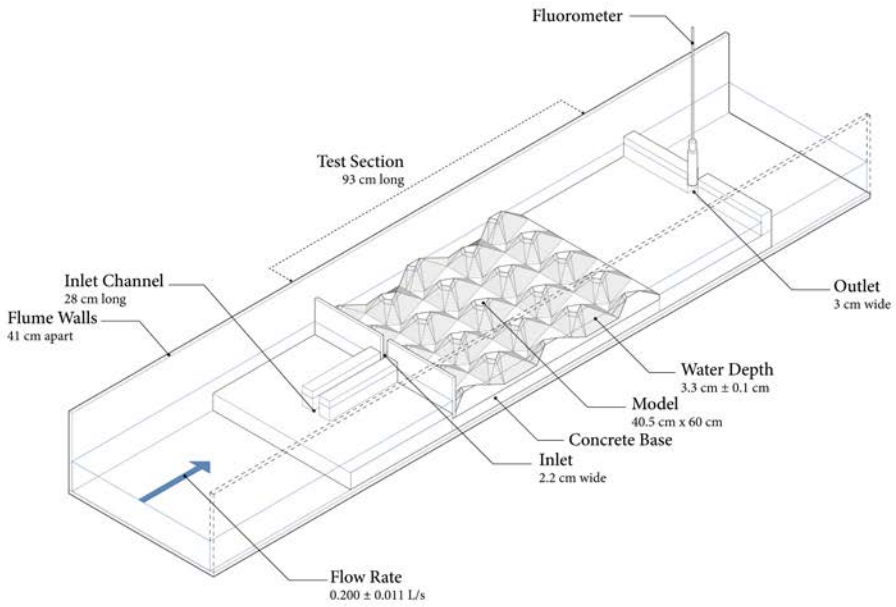

Figure 11: Experimental set-up with island topography A1, which had five rows of islands.

7.2. Tracer Testing and Hydraulic Performance Metrics

The residence time distribution of each design was measured using a standard tracer experiment. A 1 mL slug of 1:10,000 rhodamine solution was injected over less than 1 second into

the inlet channel. The concentration of tracer at the outlet, C, was measured as a function of time since release, t, using a UniLux fluorometer sampling at 1 Hz. To adequately capture the tail of the distribution, the concentration was measured for four times the nominal residence time of the open basin, $4T_{nc}$. The residence time distribution (*RTD*) was estimated from the concentration recorded at the outlet (e.g., Werner and Kadlec, 1996):

$$RTD\ (t) = \frac{QC(t)}{\int_0^\infty QC(t)dt} \tag{6}$$

Two metrics were used to compare the performance of the different topographies. First, short circuiting is associated with mass leaving the basin at times much shorter than the nominal residence time, so that a reasonable metric for short-circuiting is the time at which 10% of the injected mass has exited the basin, which was called T_{10}. To account for the loss of volume associated with the inclusion of topography, which shortens the nominal residence time, T_{10} was normalized by the nominal residence time of the open basin control, T_{10}/T_{nc}. Second, assuming a pond was operated at steady-state conditions with inflow concentration C_o and exit concentration C_e, the expected pollutant removal efficiency can be defined as C_e/C_o (e.g., Kadlec and Wallace, 2009). Assuming pollutant removal follows a first-order reaction, with rate constant k,

$$\frac{C_e}{C_0} = \int_0^\infty RTD(t)\exp(-kt)\,dt \tag{7}$$

For a consistent comparison, the rate constant was set to $k = 1/T_{nc}$ for all cases. Two replicates were conducted for each basin topography, yielding two estimates of T_{10} and C_e/C_o. Table 3 reports the mean of the replicates and the uncertainty, defined using the standard error (*SE*), which for two replicates is. the difference between replicates (e.g. Taylor, 1997). The uncertainty was taken to be 1.96 *SE* for 95% confidence. In some cases the replicate T_{10} values were identical, yielding $SE = 0$, for which the uncertainty was defined by half the sampling resolution (0.5 s). The variation in flow rate was the main contributor to the uncertaintyin estimated T_{nc} (δT_{nc} = 3 s). The uncertainties δT_{10} and δT_{nc} were combined to produce the uncertainty in the metric T_{10}/T_{nc} (Taylor, 1997),

$$\frac{\delta(T_{10}/T_{nc})}{(T_{10}/T_{nc})} = \sqrt{\left(\frac{\delta T_{10}}{T_{10}}\right)^2 + \left(\frac{\delta T_{10}}{T_{nc}}\right)^2} \quad (8)$$

Finally, streamline maps were constructed using a frame-by-frame analysis of digital video. Tracer was sequentially injected at multiple points within the basin to trace out different streamlines. The upstream movement of tracer identified regions of recirculation. Specifically, the boundary of a recirculating region was located where injections of tracer transitioned from being carried upstream (in a recirculation zone) to downstream (outside a recirculation zone).

7.3. Construction Cost

The earthwork costs (excavation, rough grading, and fine grading) were used to compare differences in construction cost between the topographies. The costs that would be the same for all topographies are intentionally excluded, e.g. the removal of excess soil and site preparation (e.g. clearing and grubbing, managing difficult soils, or dewatering). We also excluded site dependent costs, such as erosion control measures and maintenance costs. The earthwork costs were estimated for a field-scale basin 21 m wide and 47 m long and operated at a water depth of 0.8 m. The earthwork costing methodology was developed with assistance from Mark Lindley, PE, Senior Engineer at Environmental Science Associates. The earthwork costs assumed the wetland and islands were constructed below grade, requiring excavation and grading of soil. The soil volume removed to form islands was multiplied by excavation cost outlined in the RSMeans cost manual (2017) (Table 1). After excavation, two passes of rough grading shaped the islands. The surface area of each island was multiplied by the rough grading cost per area. Finally, the cost of one pass of finish grading was calculated based on the surface area of the entire site.

Table 1: Cost parameters use to estimate the earthwork cost, based on data from RSMeans (2017).

Cost Parameters			
	R.S. Means Unit Cost	Specifications	Cost
Excavation	31 23 16.46 Excavating, Bulk Dozer 2040 (page 294)	Using a dozer (80hp, 50' haul) on an open site with clay soil.	$5.60 per cubic yard
Rough Grading: 2 passes	31 22 13.20 Rough Grading Sites 0170 8100-10000 S.F., dozer (pg 282)	Using a dozer on a site 8,100-10,000 square feet	$0.16 per sq. foot for each pass
Finish Grading: 1 pass	31 22 16.10 Finish Grading 2200 Slopes, Gentle (pg 282)	Using a dozer on a site 8,100-10,000 square feet	$0.21 per sq. yard for each pass

7.4. Habitat Diversity

The habitat diversity index (H) was calculated using the Shannon-Weaver entropy measure (Shannon and Weaver 1949, Krebs 2009), which other researchers have used for the same purpose (Kearney et al. 2013, Brandt et al. 2015). Using water depth as a proxy for habitat, we measured the topographical surface area that fell into each of four habitats: upland (above water), emergent vegetation (0 to 30 cm water depth), submerged vegetation 262 (30 cm to 46 cm water depth), and open water (deeper than 46 cm). As with the construction cost, this index was calculated for each design at full scale. For N habitat zones, the habitat diversity index is

$$H = -\sum_{i=1}^{N} p_i \ln(p_i) \quad (9)$$

in which p_i is the proportion of total area occupied by the i_{th} habitat zone (e.g. Kearney et al., 2013). The maximum habitat index is

$$H_{max} = ln\ (N) \quad (10)$$

so that for N = 4 habitats, H_{max} = 1.39. The minimum value was zero, corresponding to the control because it had only one habitat zone (open water).

8. RESULTS AND DISCUSSION

8.1. Phase 1

The first phase of experiments compared simple bathymetric features (baffles, island clusters, and pinch points), using the short-circuiting parameter T_{10}/T_{nc} (Table 2). For the open

basin control $T_{10}/T_{nc} = 0.22 \pm 0.06$. This value reflected the presence of significant short-circuiting between the inlet and outlet. In some cases, the addition of topography made short-circuiting worse ($T_{10}/T_{nc} < 0.22$). In particular, every case with islands distributed along the centerline (ISL-1 to ISL-4, Figure 9) produced a lower metric, with $T_{10}/T_{nc} < 0.17$. In these cases, although the initial island deflected the inflow, which should diminish short-circuiting, the series of islands created channels along the basin edges, which became new regions of short-circuiting.

This was similar to the enhanced short-circuiting observed by Khan et al (2011) for a detention pond with a single central island.

Table 2: Phase 1 testing results

Model	Solid Volume [%]	T_{10}/T_{nc}	$\delta(T_{10}/T_{nc})$
BER-1	15	0.25	0.03
BER-2	10	0.25	0.04
BER-3	15	0.31	0.04
BER-4	10	0.20	0.04
BER-5	10	0.29	0.05
ISL-1	10	0.17	0.03
ISL-2	15	0.13	0.04
ISL-3	10	0.17	0.04
ISL-4	15	0.14	0.04
CLU-1	10	0.51	0.05
CLU-2	10	0.23	0.10
CLU-3	10	0.20	0.04
CLU-4	10	0.38	0.04
CLU-5	10	0.18	0.04
CLU-6	10	0.20	0.05
CONTROL	0	0.22	0.06
PIN-1	NA	0.25	0.06
PIN-2	NA	0.18	0.03
PIN-3	NA	0.26	0.05
PIN-4	NA	0.24	0.05

The serpentine bathymetries (BER-1 to BER-4, Fig. 1) mostly improved the hydraulic performance, consistent with previous recommendations (e.g. Thackston et al., 1987). The exception was BER-4, with baffles that did not extend past the basin centerline, and thus did not block the inlet-outlet short-circuiting path. In this case, the performance metric was T_{10}/T_{nc} = 0.20±0.04. In contrast, with the same basic geometry as BER-4, but longer baffles, BER-3 produced T_{10}/T_{nc} = 0.31±0.04, demonstrating the importance of extending 293 baffles past the basin centerline.

The pinch point series was inspired by the idea of breaking a single basin into two basins in series, which, based on tanks-in-series analysis (e.g. Fogler, 1992; Kadlec and Wallace, 2009), should improve hydraulic performance. Generally, the pinch point cases did better than the open basin, but none were top performers. The top performers, CLU-4 and CLU-1, both included island clusters located at the inlet, with T_{10}/T_{nc} = 0.38±0.04 and 0.51±0.05, respectively. These cases performed well because the first island split the inflow jet into two segments, and subsequent islands met and deflected each of the jet segments, spreading the inflow over the basin width. Because the island clusters produced the highest values of T_{10}/T_{nc}, the second phase of experiments considered more complex island clusters at the inlet.

8.2. Hydraulic Performance of Phase 2 Topographies

In the second phase, 34 topographies were tested, including an open basin and a serpentine basin for comparison. The estimated metrics for all topographies are listed in Table 3.

Table 3: Hydraulic metrics T10/Tnc and Ce/Co for phase 2 topographies (Figure 10). Uncertainty δis 95% confidence based on two replicates, as described in the Methods. The nominal residence time of the control had uncertainty δTnc = 3s.

Topography	T_{10} [s]	δ T_{10} [s]	T_{nc} [s]	T_{10}/T_{nc}	δ (T_{10}/T_{nc})	C_e/C_0	δ (C_e/C_0)	Topography Volume [cm^3]	Diversity Index
A1	28.5	0.5	69	0.41	0.02	0.506	0.010	2980	0.93
A1-Reversed	22.5	0.5	62	0.37	0.02	0.566	0.010	2980	0.93
A2	35.5	0.5	65	0.55	0.03	0.410	0.014	1446	0.59
B1	28.0	0.5	60	0.47	0.03	0.511	0.010	2235	0.79
B2	32	3	71	0.44	0.05	0.452	0.010	2733	0.90
B3	29.0	0.5	62	0.47	0.02	0.520	0.012	2999	0.96
B4	35	4	62	0.55	0.07	0.46	0.04	1576	0.59
B5	35.5	0.5	66	0.54	0.03	0.46	0.02	2037	0.71
C1	28	3	63	0.43	0.05	0.45	0.03	1096	0.46
C1A	26	4	61	0.43	0.07	0.50	0.08	832	0.38
C1A.S1	34.5	0.5	61	0.57	0.03	0.42	0.03	1001	0.44
C2	30.0	0.5	63	0.47	0.02	0.454	0.006	1665	0.63
C3	32.0	0.5	68	0.47	0.02	0.464	0.004	1508	0.59
C3.S2	32.0	1.9	59	0.54	0.04	0.48	0.02	1988	0.71
C4	30.5	0.5	67	0.46	0.02	0.440	0.010	1227	0.50
C4.S1	33.5	0.5	71	0.47	0.02	0.410	0.016	1395	0.55
C4.S2	31.0	0.5	63	0.50	0.03	0.45	0.02	1707	0.63
C5	29.0	1.9	64	0.46	0.04	0.447	0.006	1508	0.59
C5.S2	34	3	64	0.52	0.05	0.48	0.04	1988	0.71
I1	35.5	0.5	63	0.57	0.03	0.454	0.014	3181	0.99
S1	25.5	0.5	65	0.39	0.02	0.494	0.004	323	0.18
S1.S1	27.5	0.5	60	0.46	0.02	0.45	0.02	491	0.25
S1.S2	34.0	1.9	65	0.52	0.04	0.429	0.014	803	0.36
S2	26.5	0.5	63	0.42	0.02	0.479	0.016	323	0.18
S2.S1	26.0	0.5	60	0.44	0.02	0.47	0.02	491	0.25
S3	27.0	1.9	60	0.45	0.04	0.48	0.02	436	0.22
S3.S1	29.5	0.5	65	0.45	0.02	0.45	0.02	603	0.29
S4	25.0	1.9	63	0.40	0.04	0.48	0.06	548	0.27
S4.S1	33.0	1.9	59	0.56	0.04	0.432	0.002	716	0.33
S5	26.0	1.9	68	0.38	0.03	0.47	0.02	337	0.19
S5.S3	22.5	0.5	62	0.363	0.019	0.52	0.03	674	0.33
S5.S4	31.5	0.5	63	0.50	0.02	0.432	0.006	1010	0.44
SERPENTINE	26.5	0.5	62	0.43	0.02	0.484	0.002	2148	0.77
CONTROL	13.5	0.5	64	0.210	0.013	0.54	0.04	0	0

Based on the short-circuiting metric, T_{10}/T_{nc}, all of the island designs improved performance compared to the control (Figure 12a). Moreover, 23 cases produced lower values of T_{10}/T_{nc} than the serpentine design. The best performing designs were C1A.s1, which had 2 rows of similar islands, and I1, which had 5 rows of islands that decreased in size with distance from the inlet (Figure 10). Both designs achieved T_{10}/T_{nc}= 0.57±0.03. Recall that for ideal plug flow, T_{10}/T_{nc} = 1. However, this cannot be achieved with island topographies, because the addition of islands reduces the available volume, so that the effective T_n is less than T_{nc}. It is difficult, without more extensive testing, to determine the upper limit of feasible T_{10}/T_{nc} values. However, the results here do show that improvements over an open basin can be achieved with the addition of islands. Ultimately, the degree of engineering intervention selected to improve the performance of a given basin will depend on the constraints of cost and required concentration reduction.

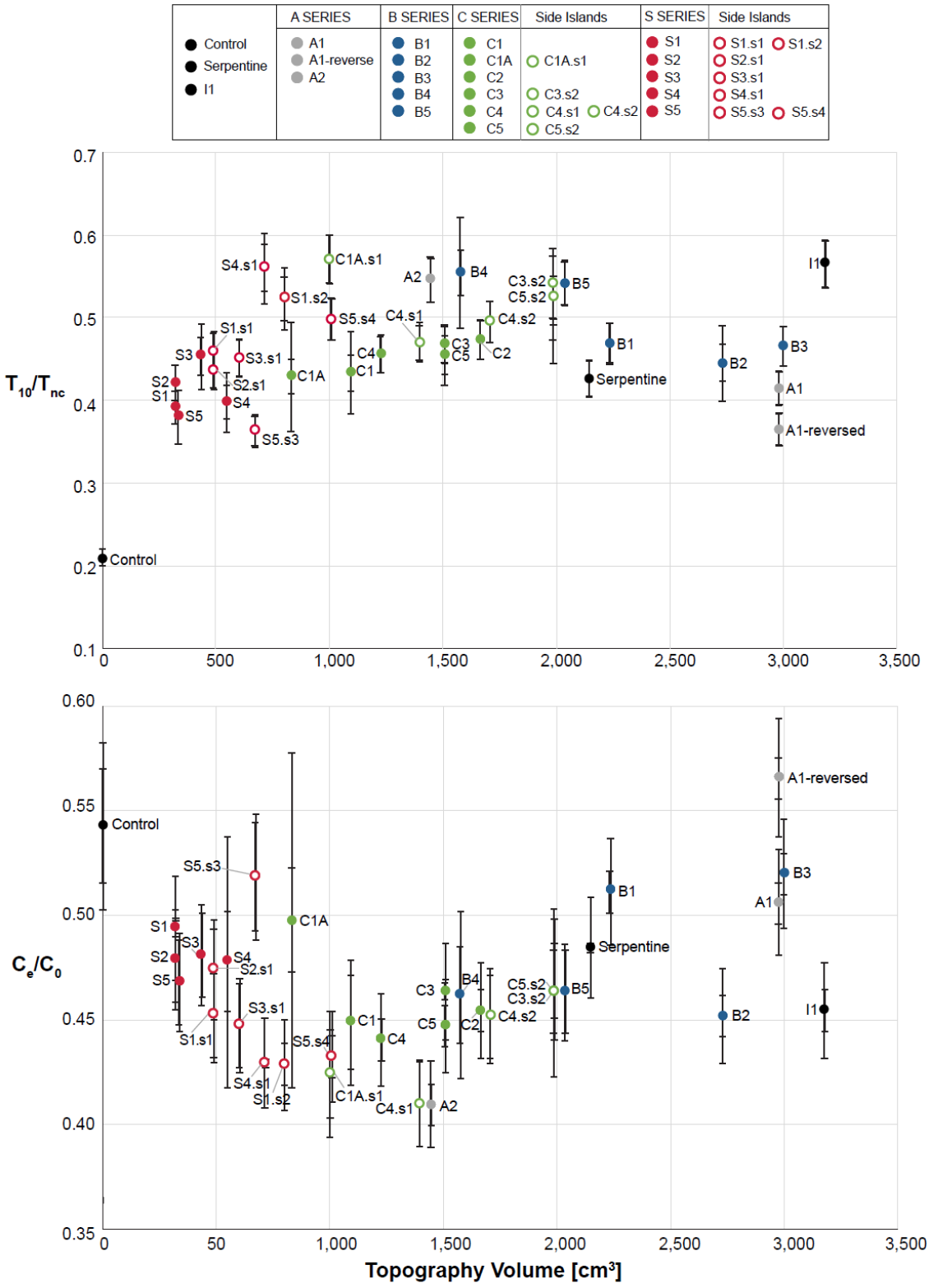

Figure 12: Performance metrics vs topography volume in scaled model. (a) T10/Tnc, metric for short circuiting. (b) Ce/Co, pollutant removal efficiency from eq. 4 and assuming rate constant k = 1/Tnc. Error bars indicate 95% confidence interval based on two replicates and the propagated uncertainty in *Tnc*.

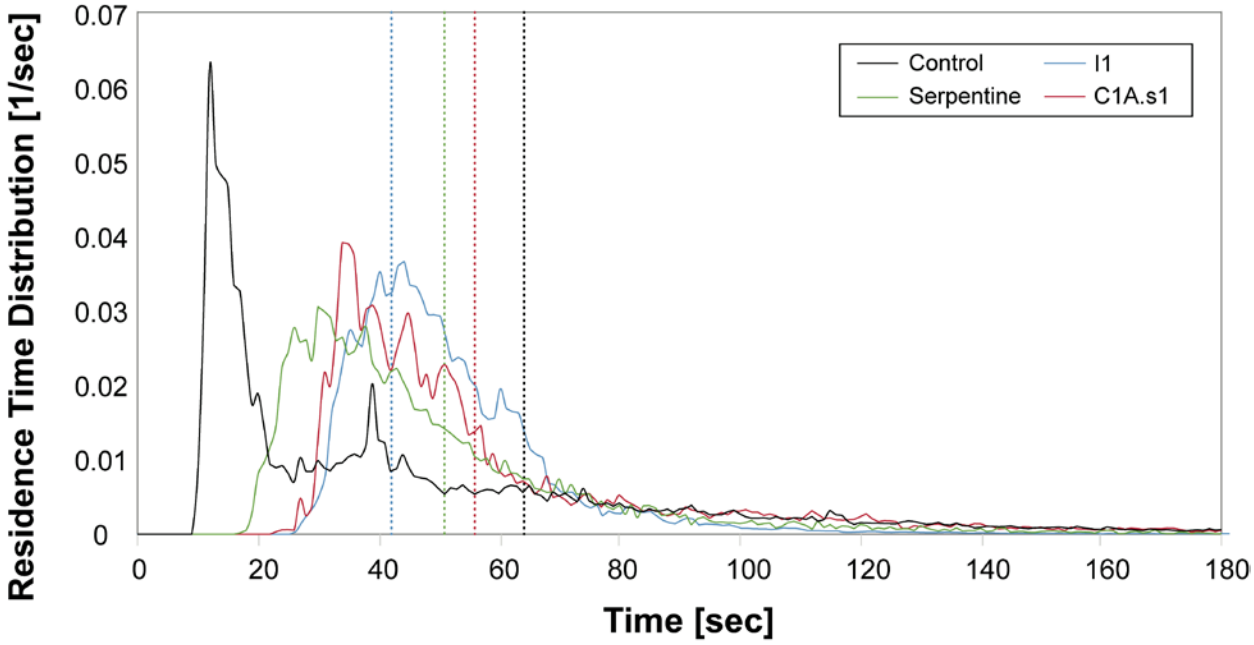

Figure 13: RTD for control (black) and serpentine (green) cases, and for the island cases with highest T10/Tnc, specifically I1 (blue) and C1A.s1 (red). Each RTD is the average of two replicates. The nominal residence time of each case, which accounts for water volume lost to island volume, is located at the vertical line of matching color.

Figure 13 compares the *RTD* for the best performing cases (I1 and C1A.s1) to the control and serpentine cases. A vertical line of matching color shows the nominal residence time of each case. When short-circuiting was present, the *RTD* peak occurred before the nominal residence time. The greatest short-circuiting occurred in the open basin (black curve in Fig. 5), with the *RTD* peak occurring long before the nominal residence time (vertical black line). The time between the peak and nominal residence time decreased for the serpentine (green) and C1A.s1 (red). The case with 5 rows of islands (I1, blue curve) was closest to plug flow, with the *RTD* peak arriving at its nominal residence time. For I1 the islands decreased in size with distance from the inlet, which smoothly spread the inflow to a laterally-uniform distribution at the end of the island sequence. Note that while similar performance was achieved by C1A.s1 and I1, both with T_{10}/T_{nc}= 0.57±0.03, I1 required more than twice the earthwork volume, showing that designers have choices amongst high-performing cases with more or less earthwork, which would have different impacts on construction cost, habitat creation, and storage volume.

Next, we considered how the difference in hydraulic performance translated into pollutant removal, indicated with C_e/C_o (Figure 12b), assuming a first-order reaction with rate constant k = $1/T_{nc}$. All of the island topographies, except for 386 A1-reversed, produced values of C_e/C_o lower

than the control (0.54±0.04). Most of the topographies produced lower values than the serpentine (0.484±0.002). Generally, cases with higher T_{10}/T_{nc} (Figure 12a) produced lower values of C_e/C_0 (Figure 12b), however, T_{10}/T_{nc} was not a perfect predictor of pollutant removal ranking. For example, the greatest concentration reduction (lowest C_e/C_o) was achieved by C4.s1and A2 (C_e/C_0 = 0.410±0.016 and 0.410±0.014, respectively), but these cases exhibited different T_{10}/T_{nc} = 0.47±0.02 and 0.55±0.03, respectively (Figure 12a). Further, the metric T_{10}/T_{nc} suggested that I1 was a top performer, but it only ranked in the middle quartile with regard to C_e/C_0 (= 0.454±0.014). This was because addition of so many islands significantly decreased the nominal residence time for I1 (42 s), relative to the open basin (63s), so that the benefit of removing the short-circuiting was offset by the loss of total water volume, which eliminated longer residence times and the removal potential they provide. This trade-off explained the occurrence of an optimum (minimum *Ce/Co*) topography volume between 1,000 and 1,500 cm^3, which corresponded to roughly 10% of the basin volume. That is, by adding a small amount of well placed island topography, short-circuiting was reduced, which removed short times from the *RTD* that are associated with high pollutant concentrations at the exit. However, adding too much topography (here, g.t. 1,500 cm^3) reduced the nominal residence time of the basin, which eliminated longer times from the *RTD*, which would be associated with the most significant pollutant removal. While the idea an optimum topography volume is physically reasonable, we caution that the metric C_e/C_o was determined using a spatially-uniform uptake rate, whereas the introduction of spatially-varying depth and vegetation habitat might produce spatial variation in uptake rate, and this additional non-linearity might shift the optimum position.

8.3. Single Islands and Single Row of Islands

The single island configurations are represented by solid red symbols in Figure 12. In every case, the introduction of a single island at the inlet reduced short-circuiting (increased T_{10}/T_{nc}) and enhanced pollutant removal (reduced C_e/C_0), relative to the open basin. The greatest improvement with regard to short-circuiting was achieved by S3 (T_{10}/T_{nc} = 0.45±0.04), a single island occupying 1/3 of the basin width, which performed better than both narrower (S1, S5) and wider (S4) single islands. Moving the island farther from the inlet did not improve the performance. Specifically, S1 (island at inlet) and S2 (island shifted downstream by one island length) had the same performance, within uncertainty (Table 3). The addition of flanking islands (open red symbols in Figure 12)

placed on either side of the central island generally improved the hydraulic performance (increased T_{10}/T_{nc}) relative to the single island without flanking islands (solid red symbols). For example, S1.s1 added flanking islands to S1, which increased T_{10}/T_{nc} from 0.39±0.02 to 0.46±0.02. The exception to this trend was S3 and S3.s1, for which T_{10}/T_{nc} was unchanged within uncertainty (Table 3). Flanking islands improved the water circulation in the following way. The central island split the inflow jet into two streams, and the flanking islands re-directed this flow into streamwise trajectories at 1/3 and 2/3 width of the basin, resulting in even flow across the basin width. Without the flanking islands, the flow deflected by the central island ran all the way to the sidewalls, creating streamwise flow concentrated near the walls, which was less uniformly distributed than the flanking island case and produced greater recirculation at the center. This difference is illustrated for S1 and S1.s1 in Figure 14. Given the positive benefits of flanking islands, additional cases considered the spacing between the central and flanking islands. Performance was improved with decreased distance between the islands.

For example, compare topographies S5.s3 and S5.s4 (Figure 15). A decrease in island spacing between S5.s3 and S5.s4 increased T_{10}/T_{nc} from 0.36±0.02 to 0.50±0.02, and decreased C_e/C_0 from 0.52±0.03 to 0.432±0.006 (Table 3, Figure 12).

8.4. Cases with Multiple Island Rows

The hydraulic improvement associated with the island topographies was not correlated with the number of island rows (Figure 16), indicating that the specific placement of islands was more important than the number of islands. In designs with multiple rows, the addition of flanking islands in the first row improved hydraulic performance only for some designs. For example, compare C1A and C1A.s1. The addition of side islands in the first row increased T_{10}/T_{nc} from 0.43±0.07 to 0.57±0.03. Similarly, for case C3 the addition of side islands in the first row, creating C3.s2, increased T_{10}/T_{nc} from 0.47±0.02 to 0.54±0.04. However, within uncertainty, the addition of islands did not improve C4 or C5. Further, within uncertainty, the addition of first row, side-islands did not reduce C_e/C_o in any of the cases (Table 3). To summarize, for cases with multiple rows, the addition of side-islands in the first row may reduce short-circuiting, but did not significantly change the potential for pollutant removal (C_e/C_o).

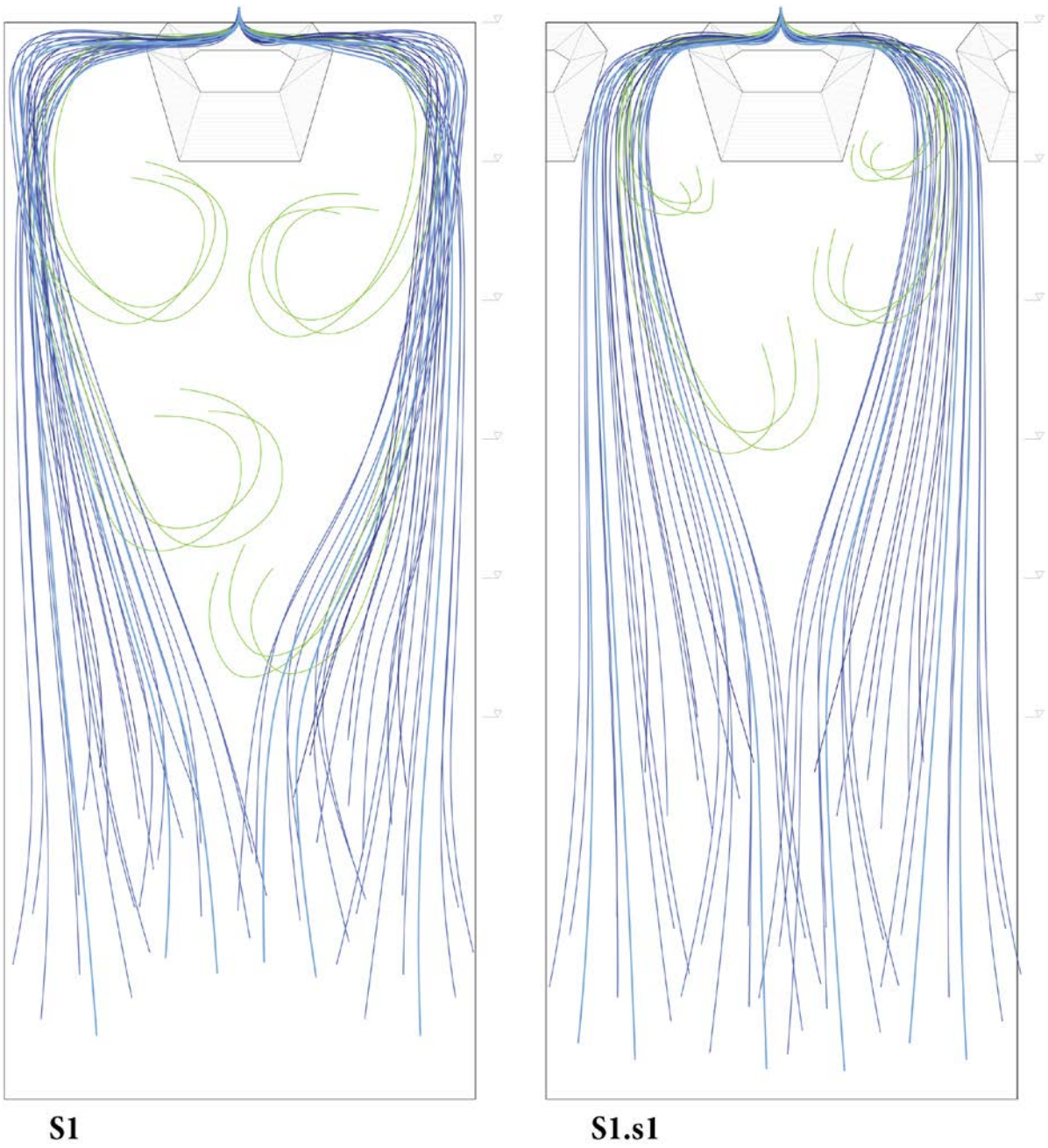

Figure 14: Circulation patterns for S1 with a single central island (left) and S1.s1 with flanking side islands (right) based on digital tracer visualization. Blue lines indicate dominant flow lines. Green lines indicate recirculation zones.

Figure 15: Circulation patterns for two cases with the same central island, but with flanking islands placed farther from center (S5.s3, left), and closer to center (S5.s4, right). Blue lines indicate dominant flow lines. Green lines indicate recirculation zones

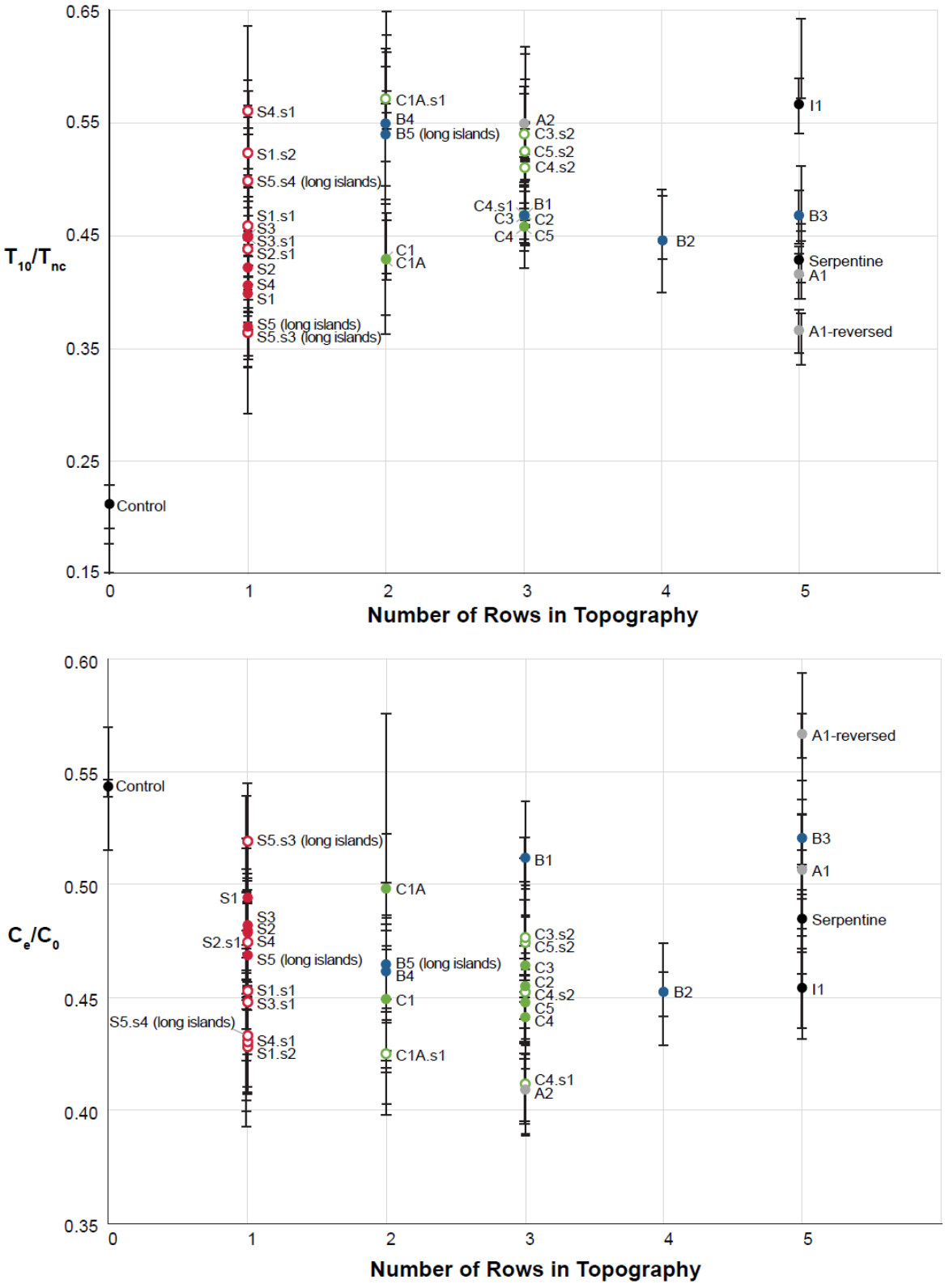

Figure 16: Performance metrics, (a) T10/Tnc and (b) Ce/Co, versus number of island rows. Error bars indicate 95% confidence interval based on two replicates and the propagated uncertainty in *Tnc*.

8.5. Streamlined Shape of Island

For most of the topographies the islands had a streamlined shape, i.e. the width of the island narrowed in the streamwise direction. A streamlined shape kept the flow from separating from the island, which was beneficial because flow separation creates recirculation and dead zones. The additional slope variation provided by the streamlined shape also contributed to emergent and submergent vegetative habitat. To confirm the hydraulic benefit of a streamlined shape, topography A1 was rotated 180° to create A1-Reversed, with the widest part of the islands closer to the inlet (Figure 10). The flow was distributed more uniformly across the basin width in A1, compared to A1-Reversed, in which the flow was directed away from the center and remained in more concentrated (narrower) flow streams (Figure 17). As a result, T_{10} was larger in the streamlined island case (A1), producing higher hydraulic performance (T_{10}/T_{nc} = 0.41±0.02), compared to A1-Reversed (T_{10}/T_{nc} = 0.36±0.02). Notably, A1-Reversed performed the worst of all cases in terms of the pollutant removal (C_e/C_0 = 0.566±0.010) and was significantly worse compared to A1 (C_e/C_0 = 0.506±0.010).

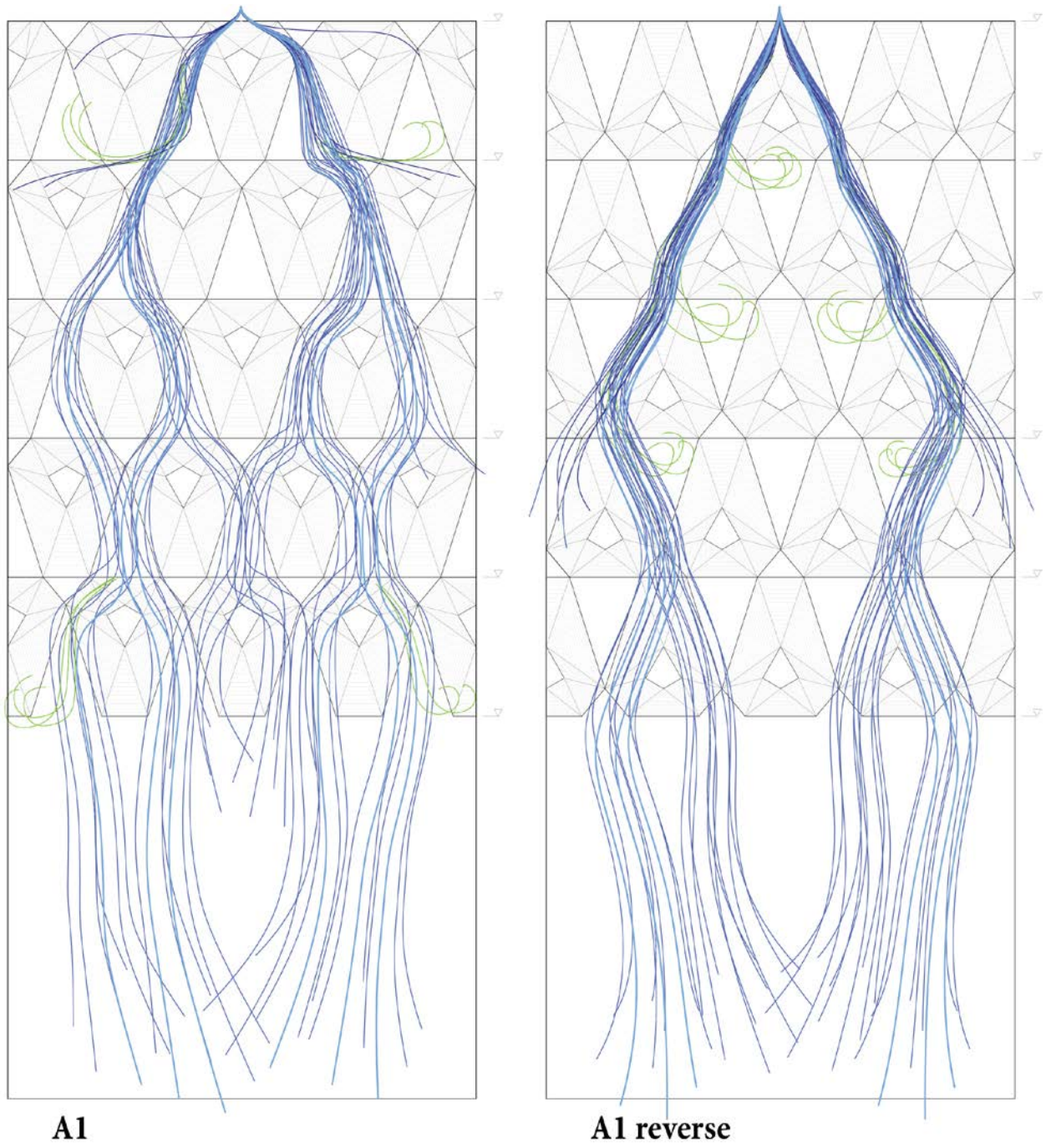

Figure 17: A comparison of flow lines for the streamlined-island case (A1, left) and the reversed-island case (A1-Reverse, right). The streamlined-islands spread the flow more uniformly across the basin width. The reversed islands direct flow away from center, creating a central dead zone that enhanced short-circuiting along the sides.

8.6. Construction Costs

The construction cost varied by only $454 across the 34 designs (Figure 18a), ranging from $7,369 (Serpentine) to $7,823 (A1). The costs were roughly equivalent for all designs because of the trade-off between excavation and island creation. Specifically, topographies with fewer islands required more excavation and less grading, while designs with more islands required less excavation but more grading. While the earthwork cost did not significantly differentiate between the designs, we caution that other costs not considered here, such as erosion control materials or maintenance, may create greater site-specific differentiation.

8.7. Habitat Creation and Optimum Design

With 4 habitats, the maximum habitat diversity index was $H_{max} = 1.39$ (eq. 6). As shown in Figure 18b, the highest scoring design was I1 ($H = 0.99$), which had the largest island volume. The lowest index was for the control, which had a uniform water depth ($H = 0$). The serpentine design scored $H = 0.77$. As expected, the habitat diversity index increased with increasing island volume(Table 3), because larger (or more) islands contributed more surface area towards habitat differentiated from open water. At the same time, larger island volume did not necessarily improve hydraulic performance defined by the metric T_{10}/T_{nc} (Figure 12). By considering both habitat creation and hydraulic performance together (Figure 18b), the island topography I1 was shown to be the best option, providing both the greatest habitat diversity as well as one of the highest values of T_{10}/T_{nc}. Given that the cost variation was not significant (Figure 18a), this design may be the optimum choice amongst the cases considered here. However, I1 has the downside of providing the least water storage volume for a given water depth.

9. CONCLUSION

The first phase of this study established that a cluster of islands near the inlet provided the greatest improvement in the short-circuiting metric T_{10}/T_{nc}. In the second phase, 34 island clusters of greater topographic complexity were explored. All 34 designs achieved higher values of short-circuiting metric (T_{10}/T_{nc}) than the basin with no topography, and 23 achieved higher values than the conventional serpentine topography. The designs offer a range of habitat potential, with habitat

diversity increasing with increasing island volume. For this reason, the optimum design in terms of the combined metrics of hydraulic performance (reduced short-circuiting) and habitat diversity was I1, a design with five rows of islands of decreasing size with distance from inlet. The construction costs did not vary significantly across the designs.

With regard to hydraulic performance alone, specifically the elimination of short circuiting, designers have several options of high performing configurations with different amounts of topography (Figure 12).

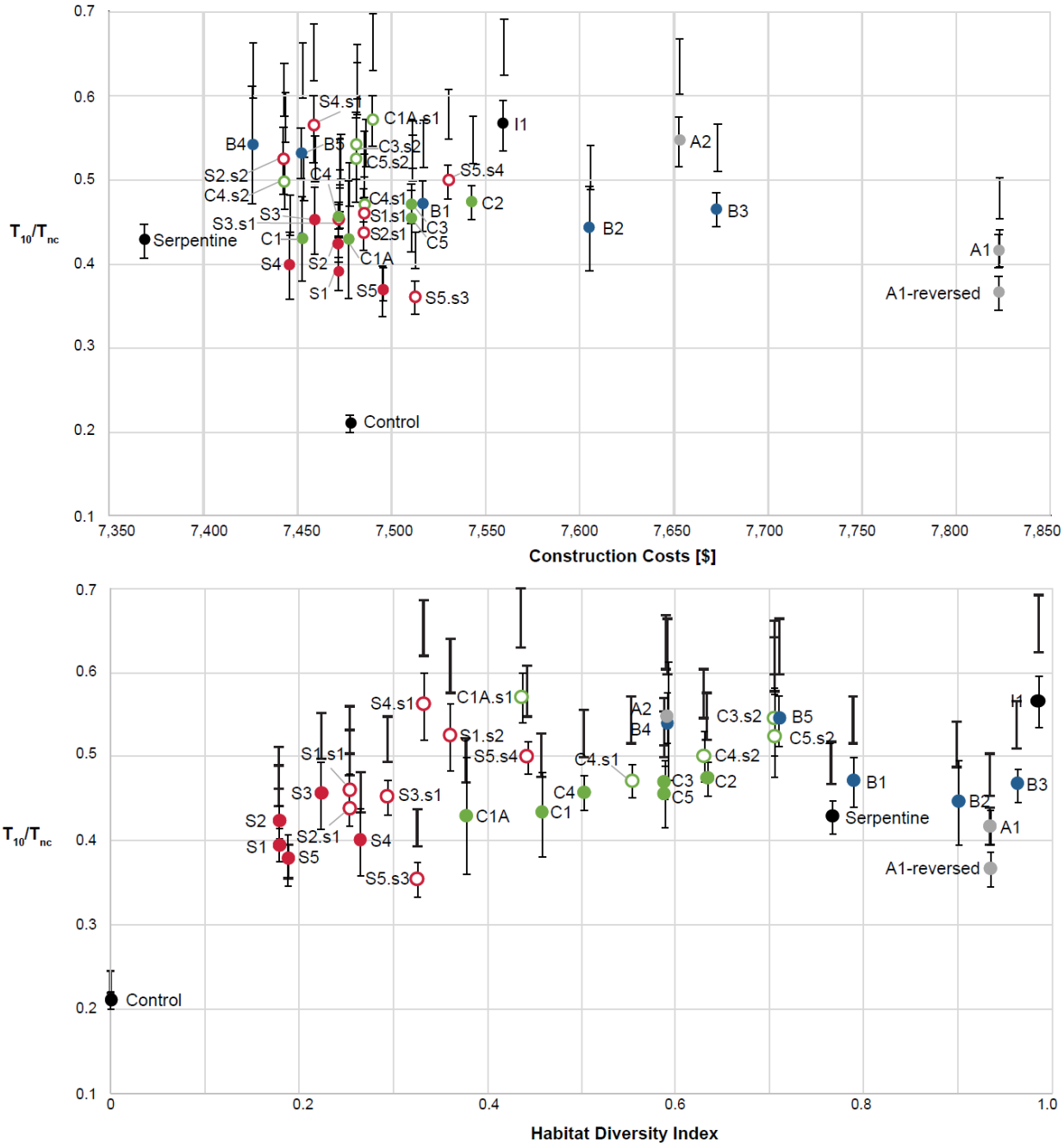

Figure 18: Comparison of (a) construction cost and (b) habitat diversity index across all designs. The error bars indicate 95% CI based on two replicates and the propagated uncertainty in Tnc.

While it may seem that these complex island forms would be difficult to build, similarly intricate landscapes for multi-functional open spaces have been recently built in Europe. In Sweden, the MAX IV Laboratory is surrounded by a radial array of hills designed to dampen ground vibrations from the adjacent road (Snøhetta 2017). In Amsterdam, the Buitenschot Land

Art Park includes a series of long, triangular mounds designed to reflect aircraft noise from the nearby Schiphol airport (H+N+S Landscape Architects 2017).

New advances in construction technology, such as GPS controlled earthmoving equipment, render such complex landscapes increasingly feasible. To conclude, previous studies have encouraged an integration of engineering and ecology (Wurth,1996; Connor and Luczak, 2002).

This study advanced the ecological basis for green infrastructure design by demonstrating the superior performance of several specific island cluster landscapes for improving both the hydraulic and ecologic function of detention ponds and treatment wetlands.

CHAPTER 3: NUMERICAL MODELING STUDY TO COMPARE THE NUTRIENT REMOVAL POTENTIAL OF DIFFERENT FLOATING TREATMENT ISLAND CONFIGURATIONS IN A STORMWATER POND

ABSTRACT

Constructed wetlands, which are commonly used in wastewater treatment, are difficult to use for stormwater treatment, because the water level variation in a stormwater pond makes it difficult for rooted vegetation to survive. As an alternative, vegetation can be grown on floating mats, called floating treatment islands (FTI), with roots extending downward into the water. Nutrient removal is achieved through uptake and trapping by the matrix of roots and bio-film. The overall treatment provided by a pond with FTIs depends on the fraction of flow exposed to the root zone. This study used numerical modeling to study the flow through the root zone, with the goal of determining which configuration of FTI achieved the greatest overall treatment. Six different configurations were considered, all with root zone volume equal to 11% of the pond volume. The permeability of the root zone was estimated using velocity measurements within real floating vegetation. A first-order removal rate within the root zone (k_r) was estimated from removal rates reported in the literature. Preliminary studies considered the similarity in flow and removal between systems of different physical scale. Geometric similarity of the root zone guaranteed flow similarity within the root zone. To achieve performance similarity (same mass reduction), systems need to have the same non-dimensional removal rate ($k_r t_n$,, with t_n the nominal residence time of the pond). The consideration of different FTI configurations showed that wakes generated by upstream FTIs lowered the mass removal of downstream FTIs, so that segmenting a single large

FTI into multiple smaller FTIs in series did not improve overall nutrient removal. However, segmenting a single FTI into a pair of parallel FTIs did improve the nutrient removal, and this configuration provided the best pond-scale removal.

Keywords: Floating Treatment Islands, Stormwater Pond, Mass Removal, Numerical Modeling

10. INTRODUCTION

Constructed wetlands with rooted plants have been integrated into urban water treatment (Carleton et al., 2001; Crowe et al., 2007; Kadlec and Wallace, 2009; Melbourne Water, 2002), because they have low-maintenance compared to traditional treatment, while also enhancing habitat and providing recreational and aesthetic value to the landscape (Knight et al., 2001; Lee and Li, 2009; Rousseau et al., 2008). This natural infrastructure is difficult to implement for stormwater treatment, because the water level in a stormwater pond varies significantly over time-scales of days and weeks, making it difficult for rooted vegetation to establish and survive (Ewing, 1996; Headley and Tanner, 2006; Greenway and Polson, 2007). Floating treatment islands (FTI) have been introduced as an alternative for stormwater treatment, because the floating vegetation can tolerate large swings in water depth (e.g. Headley and Tanner, 2012). Floating treatment wetlands are an appealing retrofit to existing stormwater ponds, because they do not require additional earthwork or land, and they do not detract from the available storage volume, because they float (Winston et al. 2013).

A floating treatment island (FTI) consists of emergent vegetation grown hydroponically on a floating mat. The roots grow into the water beneath, providing a large surface area for biofilm growth (Tanner et al 2011). The dangling roots covered with sticky biofilm are very effective in trapping fine particles. Eventually, the particles entrapped in biofilm become heavy enough to slough off and settle to the bed. This entrapment-settling mechanism is the main removal process for particulate-bound nutrients and metals within an FTI (e.g. Hoeger, 1988; Smith and Kalin, 2000; Headley and Tanner 2006; Borne 2014). Some microbial mediation also occurs, but direct uptake by the plants plays a relatively minor role (e.g. Tanner and Headley 2011, Borne 2014, Lane et al. 2016). Several previous studies have compared mesocosms or stormwater ponds with and without FTIs to evaluate the pollutant removal potential. A majority of these studies have shown increased pollutant removal associated with FTIs (e.g. Tanner and Headley, 2012, Lane et

al. 2016). For example, Tanner and Headley (2011) showed that FTIs enhanced the removal of copper, phosphorus, and fine suspended sediments. FTIs planted with *Canna flaccida* and *Juncus effusus* deployed in a trough mesocosm removed up to 75% of nitrogen and phosphorus from simulated stormwater (White and Cousins, 2013). Chang et al. (2012) compared ponds with FTIs occupying 5% and 10% of the pond surface area. While both configurations removed nutrients, unexpectedly the removal was similar for 5% and 10% surface coverage. This might be explained by differences in water circulation through the root zone. Indeed, several studies have noted that the treatment provided by individual FTIs depends on the fraction of flow that passes through the root zone, and that an understanding of this process would improve the design of FTIs for applications in rivers and detention ponds (Headley and Tanner, 2012; Chang *et al*, 2012, Pavlineri et al. 2017). The goal of this study was to use Computational Fluid Dynamics (CFD) to study the flow through FTI root zones and to analyze the impact of FTI configuration on the estimated mass removal within individual root zones.

11. METHODS

The stormwater pond geometry was chosen to match the pond described in Khan *et al* (2013), so that Kahn's measurements could be used for model validation. Kahn's experiments were done in a 1:10 scale model of a real stormwater pond located in New Zealand. The model consisted of a rectangular tank with sloping slides (2:1, horizontal:vertical) and top dimensions of length, width and depth equal to 4.1 m, 1.5 m, and 0.23 m, respectively. The inlet and outlet pipes had diameters of 45 mm and 105 mm, respectively. The geometry for all FTI configurations is given in Table 4 and shown in Figure 19. For all cases the total root zone volume was 11% of the pond volume.

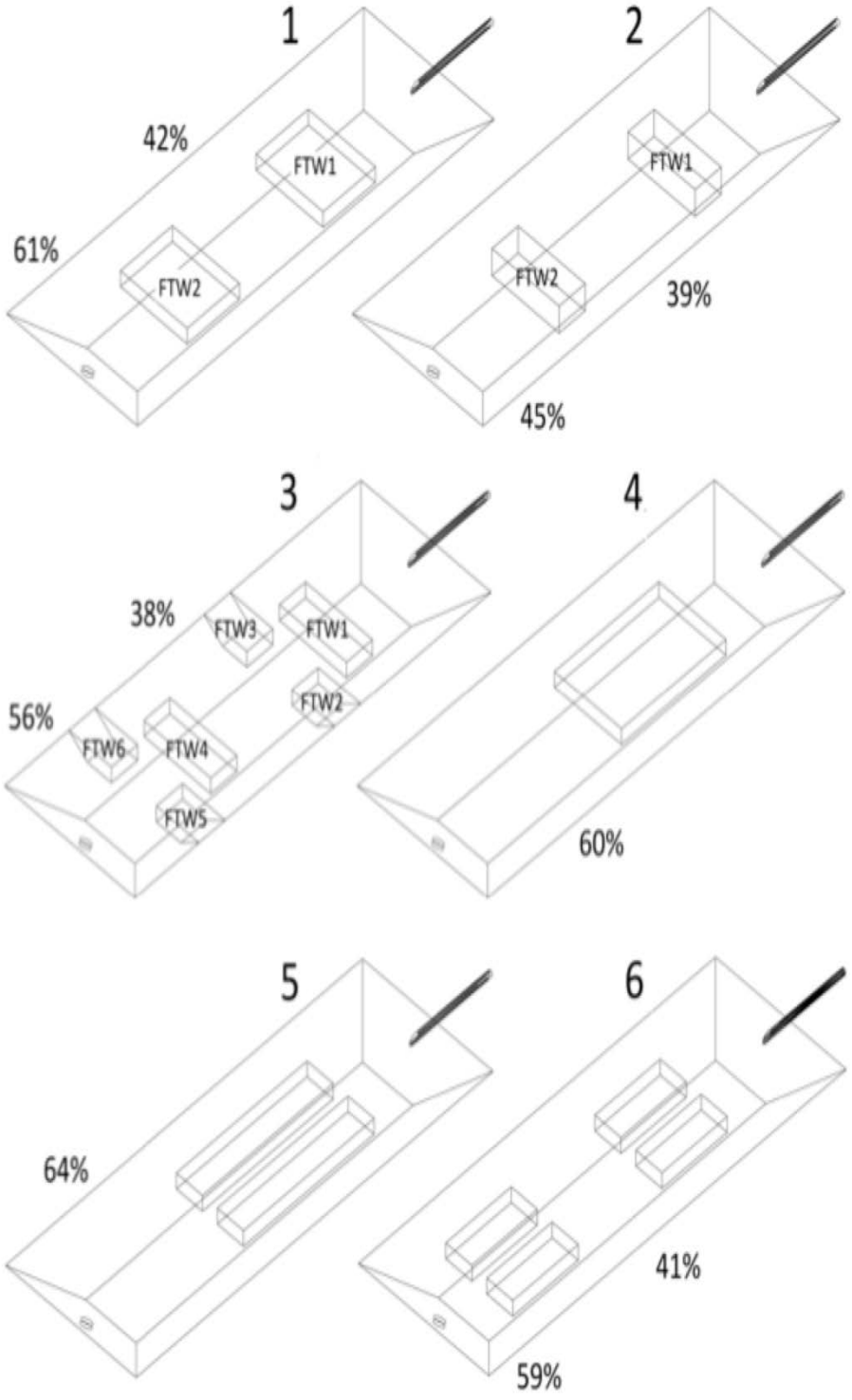

Figure 19:Geometries for the six test cases. Dimensions of individual FTI root zones given in Table 4. The black cylinder represents the inlet pipe. The bold numbers show percent of inject mass removed at the position long the pond corresponding to the number's position. For example, in case 1 the fraction of mass removed between the inlet and the downstream end of FTI1 was 42%, and between the inlet and the outlet was 61%

Table 4: Dimensions of the root zones (length, width, depth) given in meters.

	FTI1	FTI2	FTI3	FTI4	FTI5 and FTI6
Case 1	0.6, 0.77, 0.105	0.6, 0.77,	---	---	---
Case 2	0.3, 0.8, 0.2	0.3, 0.8, 0.2	---	---	---
Case 3	0.22, 0.77, 0.105	0.3,0.49,0.105	0.3,0.49,0.105	0.3,0.77,0.105	0.3, 0.49, 0.105
Case 4	1.2,0.77,0.105	---	---	---	---
Case 5	1.54, 0.3, 0.105	1.54, 0.3,	---	---	---
Case 6	0.77, 0.3, 0.105	0.77, 0.3,			

The flow field within the pond was determined using the CFD code ANSYS CFX® 17.0 with a 3D transient simulation using the Shear Stress Transport (SST) RANS (Reynolds Averaged Navier-Stokes) turbulence model. For steady, incompressible flow, the Reynolds-averaged equations for conservation of mass and momentum are, respectively:

$$\frac{\partial u_i}{\partial x_i} = 0 \tag{11}$$

$$\rho \frac{\partial u_j u_i}{\partial x_j} = -\frac{\partial p}{\partial x_i} + \mu \frac{\partial^2 u_i}{\partial x_j \partial x_j} - \rho \frac{\partial \overline{u_i' u_j'}}{\partial x_j} + S_{M,i} \tag{12}$$

in which i or j = 1, 2 or 3; x_1, x_2 and x_3 denote the streamwise (x), cross-stream (y), and vertical (z) directions, respectively; u_1, u_2 and u_3 are the corresponding time-mean velocity components; $\overline{u_i' u_j'}$ is the Reynolds stress, with u' denoting the fluctuating part of the velocity; p is the pressure; ρ is the fluid density; μ is the viscosity; and $S_{M,i}$ is a momentum sink used to represent the root zone drag.

The turbulent momentum flux was modeled using an eddy viscosity, whose value was predicted with a k_t-ω method. The specific turbulent kinetic energy, k_t(m^2s^{-2}), and dissipation rate, ω(s^{-1}) were modeled with the following equations

$$\frac{D(\rho k_t)}{Dt} = \frac{\partial}{\partial x_j}\left[(\mu + \sigma_{k2}\mu_t)\frac{\partial k}{\partial x_j}\right] + P_k - \beta^* \rho k \omega \tag{13}$$

$$\frac{D(\rho \omega)}{Dt} = \frac{\partial}{\partial x_j}\left[(\mu + \sigma_{\omega}\mu_t)\frac{\partial \omega}{\partial x_j}\right] + 2(1 - F_1)\rho\sigma_{\omega 2}\frac{1}{\omega}\frac{\partial k_t}{\partial x_j}\frac{\partial \omega}{\partial x_j} + \alpha\rho S^2 - \beta\rho\omega^2 \tag{14}$$

in which S is the invariant measure of the strain rate, and the shear production, P_k, was

$$P_K = min\left[\mu_t \frac{\partial u_i}{\partial x_j}\left(\frac{\partial u_i}{\partial x_j} + \frac{\partial u_j}{\partial x_i}\right), 10\ \beta^*\ \rho\ k_t\ \omega\right] \tag{15}$$

Blending functions F_1 and F_2 were used to smoothly transition from the standard $k_t-\omega$ model near the wall to a $k_t-\varepsilon$ model in the outer portion of the boundary layer. The blending function, F_1 was

$$F_1 = \tanh(arg_1^4) \tag{16}$$

$$arg_1 = min\left[max\left[\frac{\sqrt{k_t}}{\beta^* \omega d}, \frac{500v}{y^2 \omega}\right], \frac{4\rho\sigma_{\omega 2} k_t}{CD_{k\omega} d^2}\right] \tag{17}$$

$$CD_{k\omega} = max\left(2\rho\sigma_{\omega 2}\frac{1}{\omega}\frac{\partial k_t}{\partial x_j}\frac{\partial \omega}{\partial x_i}, 10^{-10}\right) \tag{18}$$

in which d was the distance to the nearest wall. The turbulent eddy viscosity was defined as

$$\nu_t = \frac{\mu_t}{\rho} = \frac{\alpha_1 k_t}{max(a_1\omega, SF_2)} \tag{19}$$

in which F_2 was the blending function

$$F_2 = \tanh(arg_2^2) \tag{20}$$

$$arg_2 = max\left(\frac{2\sqrt{k_t}}{\beta^* \omega y}, \frac{500\,v}{y^2\,\omega}\right) \tag{21}$$

The coefficients of the SST model were: $\beta^* = 0.09,\ a_1 = 0.31, \alpha_1 = 0.5532,\ \beta_1 = 0.075, \alpha_2 = 0.4403, \beta_2 = 0.0828, \sigma_{k1} = 1.176, \sigma_{k2} = 1, \sigma_{\omega 1} = 0.5, \sigma_{\omega 2} = 0.85616.$ More details on these coefficients can be found in Menter *et al* (2003). The Second Order Backward Euler Scheme was chosen for the transient scheme.

The following boundary conditions were defined. A uniform flow was imposed at the inlet. At the outlet, an average static reference pressure of 0 Pa was specified. A no-slip boundary condition was applied at the walls. The free surface was considered a symmetry plane with zero gradient normal to that plane (Stamou 2002). The root zone of each FTI was represented as a porous media using

$$S_{M,i} = \frac{\mu}{K_{perm}} u_i \tag{22}$$

in which K_{perm} was the permeability. The permeability in the root zone was determined by matching a hydrodynamic simulation to measurements provided in Downing-Kunz and Stacey (2012), who recorded the velocity field within and beneath a root zone of real floating vegetation (*E. crassipes,* water hyacinth). The live vegetation was placed in a 20-m long channel that was 0.6 m wide and filled to a water depth of 0.3 m. Velocity data was extracted from Figure 19 in Downing-Kunz and Stacey (2012), in which the root zone extended 0.62 m in the streamwise direction, and the root depth below surface was 0.125m. The floating vegetation filled the channel width. To determine an appropriate permeability for the root zone, the CFD model was configured to represent this channel and run with different values of K_{perm} ranging from 10^{-20} m^2 to 10^{-4} m^2. The simulated velocity was compared to the velocity profile measured within the root zone, with a good fit observe for $K_{perm} = 10^{-7}$ m^2. These values were subsequently used in all simulations.

The numerical code employed unstructured numerical grids, which permitted a very accurate representation of the boundaries (Figure 20). The grid was created by combining the sweep and the hex dominant methods (ANSYS Inc. 2016b) with finer spacing at the inlet and outlet regions and at the edges of the FTIs. The computational grids for each of the six cases had on the order of 10^5 hexahedral elements. More details of the governing equations, turbulence model, and algorithms can be found in the CFX® user's guide (ANSYS Inc. 2016a).

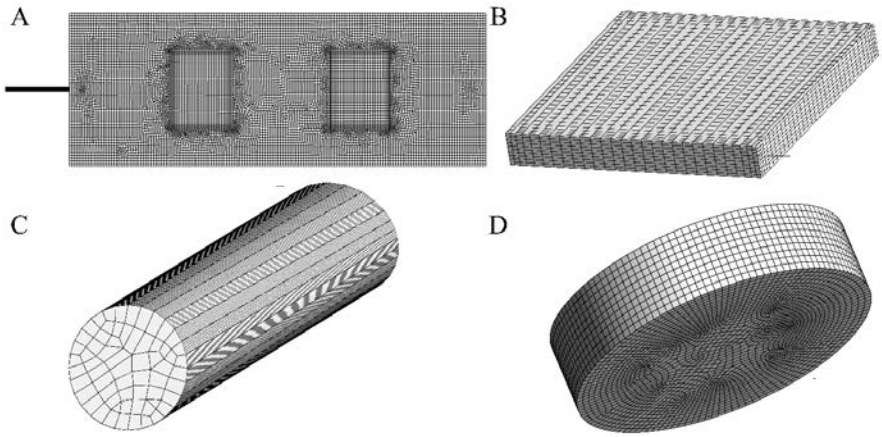

Figure 20: Examples of the mesh for components of the numerical pond model in Case 1: (A) the pond with two FTIs; (B) close up of one FTI; (C) inlet pipe; and (D) outlet pipe.

The evolution of the concentration field, C, was described using conservation of mass,

$$\frac{\partial C}{\partial t} + \frac{\partial (u_i\, C)}{\partial x_i} = \frac{\partial}{\partial x_i}\left(\frac{\upsilon_t}{Sc}\frac{\partial C}{\partial x_i}\right) - k_r C \qquad (23)$$

with turbulent Schmidt number, $Sc = (\upsilon_t / D_t)$, set to 1, which falls within the range of measured values, with D_t the turbulent diffusivity (e.g. Gualtieri et al. 2017). Removal within the root zones was represented by a first-order reaction ($k_r C$), and this term was set to zero outside the root zones. The water surface and all solid surfaces were modeled with a no-flux boundary condition. Realistic values for the first-order rate constant k_r were inferred from mesocosm studies that reported removal rate constants (k_V) for the entire mesososm volume (V_m). Assuming that mixing through the root zone was not limiting and that removal only occurred within the root zone volume (V_{root}), the rate constant within the root zone (k_r) can be estimated as $k_r = k_v(V_m/V_{root})$. Values extracted from the literature are reported in Table 5.

Table 5: Root-zone removal rates for total nitrogen estimated from measured removal within mesocosm.

Author	Vegetation	V_m/V_{root}	k_v (day^{-1})	k_r (day^{-1})
Chang et al (2012)	*Juncus Edgariae*	5.36	0.09	0.43
Chua et al (2012)	*Carex Virgata*	1.75	0.73	1.28
Chua et al (2012)	*Shoenoplectus tabernaemontani*	1.61	0.73	1.18
Chua et al (2012)	*Cyperus ustulatus*	1.47	0.73	1.07
Chua et al (2012)	*Juncus edgariae*	1.15	0.73	0.84

The simulation was validated using the physical experiments of Khan et al. (2013). Specifically, we used Case 12 in Khan, which corresponded to Case 1 in Figure 19. Khan characterized the pond circulation using the residence time distribution (RTD) determined from a standard tracer study. Tracer is introduced at the inlet as a single slug of mass, M, and the water concentration at the outlet, C_e, is recorded as a function of time, t. The RTD is then (e.g. Werner and Kadlec, 1996)

$$RTD\ (t) = \frac{QC_e(t)}{\int_0^\infty QC_e(t)dt} \tag{24}$$

Q is the pond inflow/outflow rate. The mean residence time, $t_{mean,}$ is the first moment of the RTD, and the nominal residence time is

$$t_n = \frac{V}{Q} \quad , \tag{25}$$

with V the system volume.

A numerical tracer study was conducted to determine the simulated RTD, which was then validated against the measured RTD provided in Khan et al (2013). To represent a conservative tracer in the simulation, the removal term in (13) was set to zero (k_r=0) everywhere in the domain. The simulations was set up to match the conditions in Khan et al. (2013), with flow rate Q = 1 L/s and mass M = 0.01 g injected at the inlet. This was recreated in the CFD model with a 1s injection in the inlet pipe, 720 mm upstream of the pond. The tracer concentration was monitored at the outlet to produce the RTD curve following equation 24. The simulation was run until 95% of the tracer exited the pond. The simulation was carried out using a time step that varied between 0.1

and 1 s. A smaller time step was used for the time intervals in which there was a higher variation of concentration (e.g., the tracer injection period). These time steps were chosen after a series of tests with decreasing time step showed that decreasing the time step further had no influence on the result.

After validation of the numerical model, additional simulations were run to explore different FTI configurations (Figure 19). The removal performance of each configuration was compared using a reactive tracer study, i.e. with the removal term active in equation 23. Mass M was instantaneously injected at the inlet, and the exit concentration, $C_e(t)$, was recorded. The mass escaping the pond, M_e, was then,

$$M_e = \int Q C_e dt \tag{26}$$

The fractional removal was defined as the ratio of mass escaping to mass injected,

$$\%M_e = \frac{M_e}{M} \tag{27}$$

Note that this metric is equivalent to the more common performance metric based on the steady-state outlet concentration, C_e, given a steady-state inflow concentration of C_O, i.e. steady state $C_e/C_o = \%M_e$. In some cases, it was more convenient to consider the fraction of mass removed, which is simply

$$\%M_{removed} = (1 - \%M_e) \tag{28}$$

To assess the relative contributions of different FTIs within a pond, multiple simulations were run with the removal term ($k_r C$) turned on only for selected root zones. For example, in Cases 1 through 4, the removal achieved by the first FTI in series was calculated by running the tracer simulation with removal turned on only within the first FTI (or first set of three FTIs in case 3). To assess the performance of individual FTI in series, it was necessary to account for the mass removed by upstream FTI. For this reason, the following removal efficiency was defined for an individual FTI,

$$\%M_{FTI} = \frac{(M_{in} - M_{out})}{M_{in}} \tag{29}$$

in which M_{in} and M_{out} are defined as the mass passing the cross-section directly upstream and downstream, respectively, of the FTI. Finally, to illustrate the flow within individual root zones, an bulk streamwise velocity within the root zone (U_{root}) was calculated by averaging over vertical slices (y-z plane) within the root zone and at different distances (x) from the leading edge of the root zone. The value of U_{root} at the leading edge of the root zone was denoted as U_o.

12. RESULTS AND DISCUSSION

12.1. Model Validation

The numerical model predicted the measured RTD with good agreement, as shown in Figure 21. The simulated mean residence time, t_{mean} =721.5s, was nearly identical to the experimental value of 721.7 s. The peak arrival time was also nearly identical at 400.6 s and 408.6 s for the experiment and CFD, respectively.

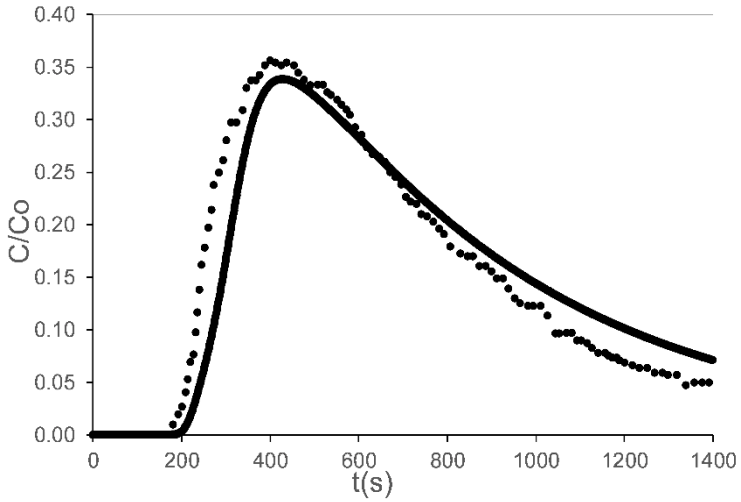

Figure 21: Comparison between simulated (solid line) and experimental (dots) tracer concentration at the outlet, C, normalized by C_o = M/V for Case 12 in Khan et al. (2013). For a constant flow rate, Q, which is valid here, the curve is a surrogate for the RTD.

12.2. Flow and Performance Similarity

To relate simulation results to real systems at different physical scale, we must understand the similarity between systems of different scale. If the Reynolds number is high enough (> 2000) to ensure inertia-dominated flow at the pond-scale, which is true for all cases considered here, the pond-scale circulation pattern will be similar between systems of different physical scale, once

normalized by the inflow velocity. However, flow within the root zone is drag-dominated, so we cannot appeal to Reynolds number similarity. Flow entering a porous layer is decelerated by the high drag within the layer over length X_D. As flow decelerates within the layer, conservation of mass requires that some flow be deflected out of the layer. For a layer with high root density, called high flow blockage, X_D is set by the cross-stream dimension of the porous layer (Rominger and Nepf 2011, Chen et al. 2013). In this study the root zone has two cross-stream dimensions (width, w, and depth h), so that $X_D \sim \min(h, w)$. Assuming the root zones represent high-flow blockage regimes, the ratio X_D/h (or X_D/w) will be the same for any scale of geometrically-similar root zone. The high-flow blockage scaling was confirmed through simulation. For each root zone, the streamwise velocity within the root zone, U_{root}, decreased with increasing distance from the leading edge (Figure 22a). As the streamwise velocity within the root zone decreased, flow exited the root zone predominantly through the bottom interface (Figure 22b). In all cases, with different values of h (Table 4), the flow decreased to zero, or reached a constant value at $x/h \approx 1$, indicating that the adjustment length was set by the root depth, X_D = h.

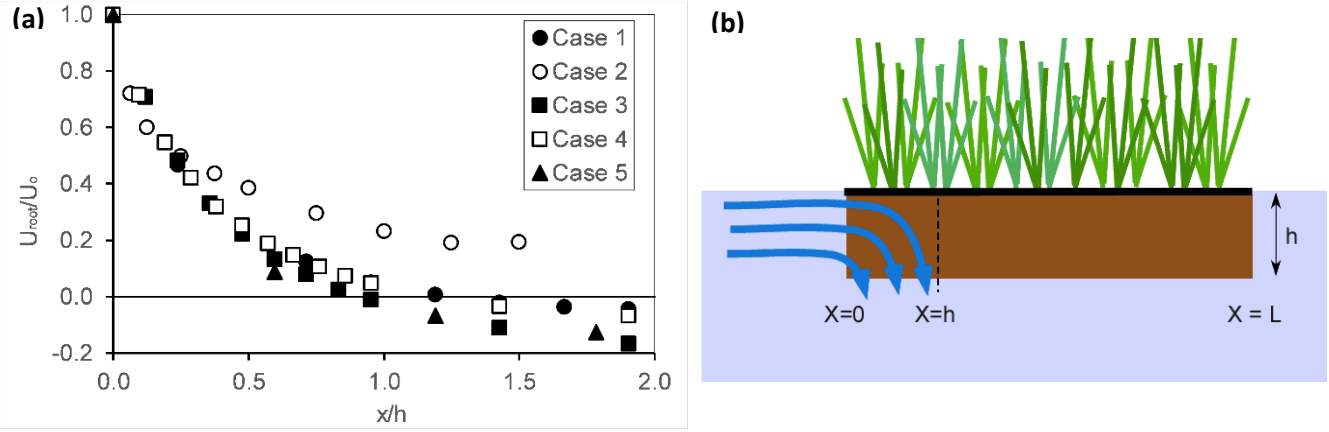

Figure 22:(a) Root-zone-average velocity, U_root, normalized by average velocity at the root-zone leading edge, U_o, as a function of distance from leading edge of the root zone (x) normalized by the root depth (h). Data shown for the most upstream FTI in cases 1 to 5. (b) Schematic of flow entering leading edge of root zone. Flow decelerates upon entering root zon, and is deflected out of root zone over distance $X_D = h$.

To confirm the flow similarity across physical scale, we ran an additional simulation for a full-scale version of Case 1, with dimensions of 41m, 15m and 2.3m for length, width and depth respectively, as reported in Khan et al (2013). The geometry of the velocity vectors was nearly

identical in the lab- and full-scale simulations, both in the open regions of the flow and within the root zones. Specifically, the length-scale of flow deceleration in the root zone was X_D/h = 1.2±0.1 and 1.3±0.1 in the lab- and full-scale simulations, respectively. We also confirmed that flow similarity ensured performance similarity. The pond removal was calculated at both scales using tracer simulations with the same non-dimensional root zone removal rate, k_r t_n = 60. The lab-scale and full-scale simulations yielded nearly identical performance, $\%M_e$ = 15 and 14 %, respectively. The similarity in mass removal for the lab- and field-scale simulation confirmed that the appropriate removal rate to achieve similarity between systems of different physical scale is determined by the non-dimensional removal rate (k_r t_n). That is, to produce the same mass removal in geometrically similar systems of different physical scale (and different t_n) one must match the non-dimensional removal rate (same $k_r t_n$). Using this similarity, one can predict the performance of geometrically similar ponds at different physical scale.

Using Case 1 as an example, the fraction of mass leaving the pond, $\%M_e$, decreased with increasing non-dimensional removal rate (Figure 23). For comparison, this figure shows both the removal achieved by the first FTI (filled circles) and the total removal achieved by both FTIs (open circles). For this configuration, FTI1 provided more mass removal than FTI2, with FTI1 achieving 60 to 70% of the total mass removal at each condition. Because we have confirmed flow similarity at the pond-scale and root-scale, Figure 23 can be used to infer the performance of systems of different physical scale. Field-scale residence times reported in the literature range from 1 to 16 days (summarized in Headley and Tanner 2012). Combining with the estimated k_r values (Table 5), full-scale ponds fall into the range of normalized removal rates of k_r t_n = 0.43 to 20. The grey box in Figure 23 marks this range. From this analysis, we infer that the configuration in case 1 could provide between 5% (t_n = 1 day) and 65% (t_n = 16 day) mass removal at the field scale.

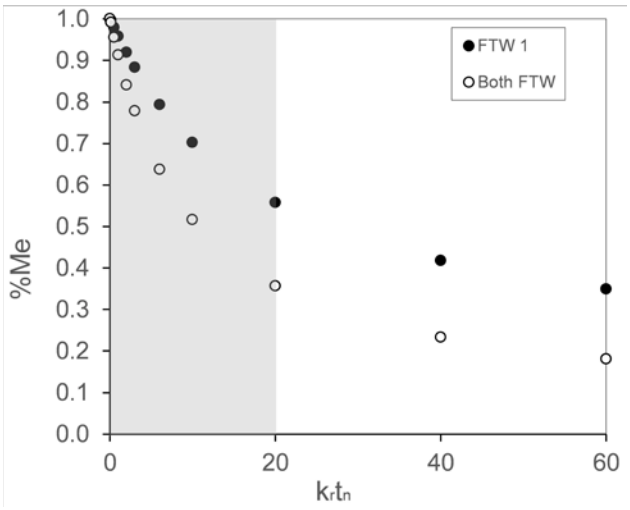

Figure 23: Percentage of mass leaving the pond, %Me, as a function of kr tn for Case 1. The removal achieved by the first FTI shown with filled circles, and the total removal achieved by both FTIs shown with open circles. The grey box represents the range of $k_r\ t_n$ expected in real ponds based on values found in the literature.

At high values of $k_r\ t_n$ all mass entering a root zone will be removed, so that the overall mass removal achieved by the pond will be limited by the fraction of mass that passes through the root zone. To demonstrate this, consider just the removal by FTI1 (black circles in Figure 23). The inflow into FTI1 occurred mainly through the front face, so that the mass entering FTI1 can be estimated by integrating uC over the front face and over time [$\iint uC\ dA\ dt$]. This indicated that 69% of mass entering the pond entered the root zone of FTI1. The maximum pond-scale removal would occur if all mass entering the root zone were taken up, which, if only FTI1 were active, would produce $\%M_e = 0.31$. This a reasonable fit for the asymptote for FTI1 (black symbols in Figure 23). It is important to note that the position of the inflow jet relative to FTI1 (Figure 19) drives this high fraction of inflow mass into the root zone. In contrast, less mass enters the root zone if the approaching flow is uniform channel flow. Specifically, consider the flow conditions studied by Downing-Kunz and Stacey (2012), in which upstream flow approached the root zone as a uniformly distributed channel flow. Simulations with this configuration showed that only 30% of the mass approaching the root zone entered the root zone, so that less removal would be expected with this configuration. This comparison illustrated an important design element. Positioning the first FTI close to a concentrated inflow jet enhanced mass flux into the root zone, which would likely enhance mass removal.

12.3. Comparison of FTI Configurations

12.3.1. Single FTI and FTI in Series

When FTI were positioned in series, the mass reduction achieved by the first FTI was always greater than that achieved by the second FTI. For example, in case 1 FTI1 removed 42% of the inlet mass, and FTI2 removed just 19% (Figure 23). The lower mass removal achieved in the downstream FTI was due in part to the first-order reaction, *i.e.* because the downstream FTI received less mass, it also removed less mass. To examine the FTI specific removal, $\%M_{FTI}$ considers the mass removed normalized by the mass arriving at a specific FTI (see eq. 22 in Methods), which corrected for the fact that downstream FTI were exposed to lower concentration. However, even with this correction, the downstream FTI removed a smaller fraction of the mass it received, compared to the first FTI in series (Table 6). The lower mass removal in the downstream FTI was correlated with a lower fraction of inflow entering the downstream FTI (Figure 24, black dots). That is, if less flow entered the FTI, less removal occurred. The downstream FTIs removed less mass because they were located in the wakes of the upstream FTI, which diminished the velocity approaching the downstream FTI, which in turn diminished the flow entering the downstream FTI (Table 6). The conclusion drawn from this series of cases (Table 6) was that breaking a single large FTI into smaller FTIs in series did not improve the mass removal, because the upstream FTI created wakes that diminished the performance of the downstream FTI. If FTI were to be implemented in series, the downstream FTI should be spaced far enough apart to avoid wakes of upstream FTI.

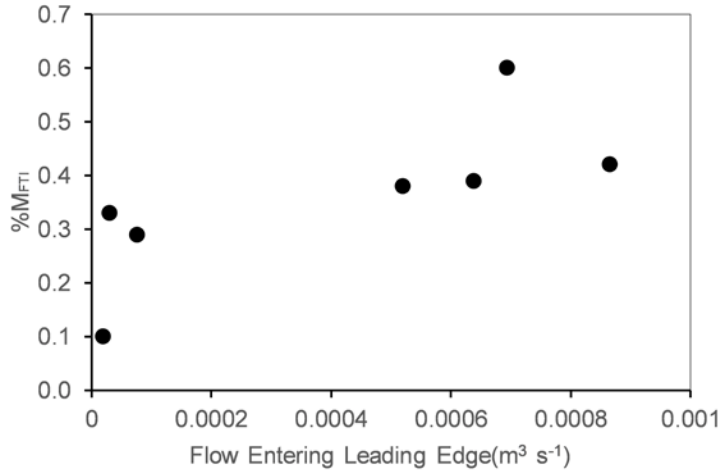

.

Figure 24: Individual FTI removal efficiency, %MFTI , increased as the flow entering the leading edge of the root zone increased. Data from Cases 1 to 4

Table 6: Flow rate entering and mass removal achieved by individual FTI.

Case	$\%M_{FTI}$ eq. 19	Flow rate entering FTI ($m^3 s^{-1}$)
1 - FTI 1	0.42	8.7 E-04
1 - FTI 2	0.33	3.1 E-05
2 - FTI 1	0.39	6.4 E-04
2 - FTI 2	0.10	2.0 E-05
3 - FTI set 1	0.38	5.2 E-04
3 - FTI set 2	0.29	7.7 E-05
4	0.60	6.9 E-04

12.3.2. FTI in Parallel

Case 5 produced the highest removal (64% removal). Cases 5 and 6 were distinct in that the islands were laid out in parallel, not in series. The inlet jet entered the FTI region through the space in between the two FTIs. Considering Case 5 with two FTI in parallel, the streamwise flow measured within the root zones showed three distinct regions. First, flow entering the leading edge decelerated over distance $X_D \approx h$ = 0.105 m, corresponding to x/L = 0.07 (Figure 25). Over this distance all of the flow entering the leading edge was deflected out of the root zone, so that the flow in the root zone reached zero at X_D. Immediately downstream of this, the flow in the root zone was reversed (moving upstream) over the distance x/L = 0.07 to 0.6. Rominger and Nepf (2011) also observed flow reversal within high flow-blockage porous layers and attributed it to the adverse pressure gradient developed at the leading edge. In the present case, elevated velocity generated between the two root zones at the leading edge produced a local low-pressure, creating a reversed pressure gradient within the root zone. Because flow inertia within the root zone was low, the flow reversed in response to this locally adverse pressure gradient. This is similar to the flow separation and recirculation generated by local adverse pressure gradients developed around solid obstructions. This phenomenon has also been observed near the leading edge of dense terrestrial canopies (Krzikalla, 2005). Finally, at the trailing edge of the root zone (x/L = 0.6 to 1) the flow was again in the positive direction, but of relatively small magnitude, compared to the region of flow reversal.

The removal achieved by each velocity zone was estimated by progressively turning on the first-order reaction in the tracer simulation (k_rC in eq. 16). The region of

reversed flow provided the most removal (36% of injected mass), compared to just (10%) and (18%) within the leading and trailing edges, respectively. That is, the highest removal was achieved in the zone with the highest flow (Figure 25). Consistent with Figure 21, this again indicated that the removal within the root zone was controlled by the supply of water into the root zone, with the highest removal achieved in the regions with greatest flushing. Finally, case 6 explored the combination of FTI in parallel and in series. The removal for this case was smaller than case 5, consistent with the conclusions drawn in section 2.1. Specifically, splitting a single larger FTI into smaller islands in series did not improve removal.

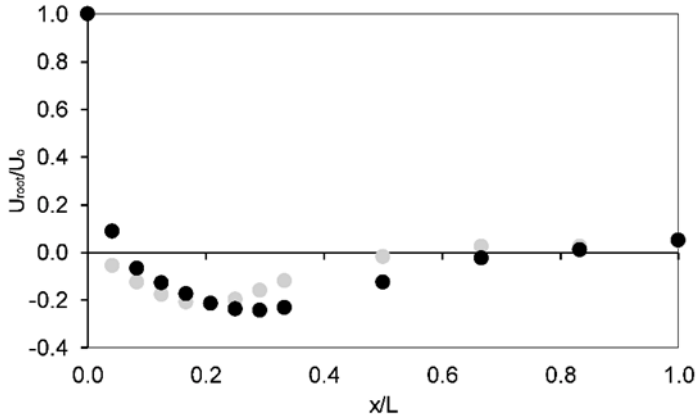

Figure 25: Streamwise distribution of streamwise velocity through the root zone, Uroot, normalized by the velocity at the leading edge, Uo, for case 5. The right and left-hand FTI depicted with black and gray symbols, respectively.

13. CONCLUSIONS

This study used numerical simulation to study the factors controlling flow and mass removal in detention ponds with floating treatment islands. In these systems, the basin-scale flow is inertia dominated, but the root-zone flow is drag dominated. The flow distribution in a root zone is determined by root zone geometry, such that geometric similarity between systems ensures similarity in root zone flow. Further, to achieve performance similarity (same mass reduction) two systems must have the same non-dimensional root zone removal rate ($k_r t_{n,}$). These scaling rules were confirmed through a comparison of flow and mass reduction between geometrically similar systems at different physical scale.

A study of six different FTI configurations of equal total root volume revealed the following concepts that can inform the better design of future FTI applications. First, through all configurations, higher removal was achieved by the FTI or portion of FTI with the highest flow rate within the root zone. This confirmed that the removal achieved by FTI is controlled by the magnitude of flow through the root zone, as previously suggested Headley and Tanner (2012). Second, the segmentation of a single large FTI into multiple smaller FTI arranged in series reduced the pond-scale removal. This trend arose because the wakes generated by upstream FTIs reduced the flow impinging on the downstream FTIs, which reduced the flow passing into the downstream root zones, which in turn reduced the removal achieved by the downstream FTIs. If FTIs are to be implemented in series, the downstream FTI should be spaced far enough away to avoid wakes of upstream FTI. Finally, parallel arrangements of FTI provided greater mass removal than single FTI or FTI in series, with the greatest mass removal achieved by a single pair of FTI configured in parallel.

NEXT STEPS

The next steps for the project are investigating the permeability of FTIs and study the role of sedimentation in the overall system performance

The permeability study will allow for a more precise construction of FTIs, by pinpointing the optimal permeability for the FTI and how it correlates with the amount vegetation needed to reproduce that permeability, the construction of the FTW system (matress+vegetation) will become cheaper and system more efficient. The initial results for this study are presented in Table 7.

The sedimentation study will allow the determintation of which process has the largest impact on the system performance (sedimentation or the FTIs) and from that, how to design a system that optimizes both.

These four studies combined will yield an optimal pond-FTI system that will take into consideration the pond topography, FTI spacial arrangement, the amount of vegetation needed for the FTI to achieve the desired performance and how it can be used to optimize sedimentation processes.

Table 7: Initial results for the permeability analysis.

Permeability (m^2)	Residence Time (s)	t_{10} (s)	Θ_{10}	$\%M_E$
1*10^1	762.24	146	0.1644	66.78
1*10^2	762.23	146	0.1644	66.77
1*10^3	762.12	145	0.1633	66.70
1*10^4	757.97	146	0.1644	66.51
1*10^5	766.20	163	0.1836	54.37
5.5*10^5	763.92	172	0.1937	66.27
8*10^5	760.05	152	0.1712	66.58
1*10^6	805.39	355	0.3998	59.55
1*10^7	799.36	335	0.3773	59.74
1*10^8	794.65	320	0.3604	60.50
1*10^9	784.61	314	0.3536	60.30
1*10^10	793.06	313	0.3525	60.24
1*10^20	793.03	313	0.3525	60.23
Empty channel	798.11	144.00	0.1622	null

REFERENCES

Abdelrhman, M.A. Effect of eelgrass *Zostera marina* canopies on flow and transport. *Marine Ecology Progress Series*, v. 248, 2003, p. 67-83.

Adamsson, Å., L. Bergdahl, and M. Vikström. 2002. A Laboratory Study of the Effect of an and Ponds. Water Science and Technology 40 (3): 291–300. doi:10.1016/S0273-1223(99)00448-5.

ANSYS Inc., 2016a. CFX-Pre-Users Guide Release 17.0.

ANSYS Inc., 2016b. Meshing Users Guide Release 17.0.

Atkins, Inc. 2015. Flood Loss Avoidance Benefits of Green Infrastructure for Stormwater Basins. J. Environmental Engineering, 113 (6): 1319–32.

Atkins, Inc. 2015. Flood Loss Avoidance Benefits of Green Infrastructure for Stormwater Management. U.S. Environmental Protection Agency, https://www.epa.gov/sites/production/files/2016-05/documents/flood-avoidance-green

Balderas, C. G., Cohen, S., Machado Xavier, M. L., Swigle, T., Qiu, W., and Nepf, H., 2017. Island Topographies to Reduce Short-Circuiting in Stormwater Detention Ponds and Treatment Wetlands. *Ecological Engineering* (to be published).

Boothroyd, R.J.; Hardy, R.J.; Warburton, J.; Marjoribanks, T.I. The importance of accurately representing submerged vegetation morphology in the numerical prediction of complex river flow. *Earth Surface Processes and Landforms*, v. 41, 2016, p. 567-576.
Borne, K.E. 2014, Floating treatment wetland influences on the fate and removal performance of phosphorus in stormwater retention ponds. *Ecol. Eng*., 69, 76–82.

Bouma, T.J.; Van Duren, L.A.; Temmerman, S.; Claverie, T.; Blanco-Garcia, A.; Ysebaert, T.; Herman, P.M.J. Spatial flow and sedimentation patterns within patches of epibenthic structures: Combining field, flume and modelling experiments. *Continental Shelf Research*, v. 27, 2007, p. 1020-1045.

Brandt, E., J. Petersen, J. Grossman, G. Allen, and D. Benzing. 2015. Relationships between Spatial Metrics and Plant Diversity in Constructed Freshwater Wetlands. *PLOS ONE* 10 (8): e0135917. doi:10.1371/journal.pone.0135917.
Carleton, J., T. Grizzard, A. Godrej, and H. Post. 2001. Factors affecting the performance of stormwater treatment wetlands. *Water Research*, 35, 1552–1562.

Chang, K.; Constantinescu, G. Numerical investigation of flow and turbulence structure through and around a circular array of rigid cylinders. *Journal of Fluid Mechanics*, v. 776, 2015, p. 161-199.

Chang, N., K. Islam, Z. Marimon, and M. Wanielista. 2012. Assessing biological and chemical signatures related to nutrient removal by floating islands in stormwater mesocosms. *Chemosphere*, *88*:736-743.

Chen, Z., C. Jiang, and H. Nepf. 2013. Flow adjustment at the leading edge of a submerged aquatic canopy. *Water Res. Res*, doi:10.1002/wrcr.20403.

Chen, Z., Ortiz, A., Zong, L., Nepf, H., 2012. The wake structure behind a porous

obstruction and its implications for deposition near a finite patch of emergent vegetation. *Water Research*, 48.

Chua, L., S. Tan, C. Sim, and M. Goyal. 2012. Treatment of baseflow from an urban catchment by a floating wetland system. *Ecological Engineering*, *49*:170-180.

Connop, S., P. Vandergert, B. Eisenberg, M. Collier, C. Nash, J. Clough, and D. Newport. 2016. Renaturing Cities Using a Regionally-Focused Biodiversity-Led Multifunctional Benefits Approach to Urban Green Infrastructure. *Environmental Science and Policy*, 62 (August): 99–111.

Connor, M.A., and A. Luczak. 2002. Designing Wetland Treatment Systems That Contribute to Wildlife Conservation. In *Proceedings of the Eighth International Conference on Wetland Systems for Water Pollution Control*, 2: 1024–37.

Costanza, R.; D'arge, R.; De Groot, R.; Farber, S.; Grasso, M.; Hannon, B.; Limburg, K.; Naeem, S.; O'neill, R.V.; Paruelo, J.; Raskin, R.G.; Sutton, P.; Van Den Belt, M. The value of the world's ecosystem services and natural capital. *Nature*, v. 387, 1997, p. 253-260.

Cotton, J.A.; Wharton, G.; Bass, J.A.B.; Heppell, C.M.; Wotton, C.S. The effects of seasonal changes to in-stream vegetation cover on patterns of flow and accumulation of sediment. *Geomorphology*, v. 77, 2006, p. 320-334.

Crowe, A., Q. Rochfort, K. Exall and J. Marsalek. 2007. Controlling urban stormwater by constructed wetlands: A Canadian perspective. *International Journal of Water*, 3:214–230.

CWNS 2008 Report to Congress | Clean Watersheds Needs Survey | US EPA," accessed January 25, 2015, http://water.epa.gov/scitech/datait/databases/cwns/2008reportdata.cfm; American Society of Civil Engineers, *2013 Report Card For America's Infrastructure*, 2013, http://www.infrastructurereportcard.org.doi:10.1016/j.desal.2006.09.034.

De Lima, P.H.S.; Janzen, J.G.; Nepf, H.M. Flow patterns around two neighboring patches of emergent vegetation and possible implications for deposition and vegetation growth. *Environmental Fluid Mechanics*, v. 15, n. 4, 2015, p. 881-898.

Defina, A.; Bixio, A.C. Mean flow and turbulence in vegetated open channel flow. *Water Resources Research*, v. 41, W07006, 2005.

Dewals, B., S. Kantoush, S. Erpicum, M. Pirotton, and A. Schleiss. 2008. Experimental and Numerical Analysis of Flow Instabilities in Rectangular Shallow Basins. *Environmental Fluid Mechanics*, 8 (1): 31–54. doi:10.1007/s10652-008-9053-z.

Dierberg, F., J. Juston, T. DeBusk, K. Pietro, and B. Gu. 2005. Relationship between Hydraulic Efficiency and Phosphorus Removal in a Submerged Aquatic Vegetation-Dominated Treatment Wetland. *Ecological Engineering*, 25 (1): 9–23.

Downing-Kunz, M.A.; Stacey, M.T. Observations of mean and turbulent flow structure in a free-floating macrophyte root canopy. *Limnology and Oceanography – Fluids and Environments*, v. 2, 2012, p. 67-79.

Dufresne, M., B. Dewals, S. Erpicum, P. Archambeau, and M. Pirotton. 2010. Experimental Investigation of Flow Pattern and Sediment Deposition in Rectangular Shallow Reservoirs. Int. Journal Sediment Research 25: 258–70. doi:10.1016/S1001-6279(10)60043-1.

Elmqvist, T., M. Fragkias, J. Goodness, B. Güneralp, P. Marcotullio, R. McDonald, S. Parnell, et al., eds. 2013. *Urbanization, Biodiversity and Ecosystem Services: Challenges and Opportunities*. Dordrecht: Springer Netherlands. doi:10.1007/978-94-007-7088-1. Emerging Principles in Landscape Ecology. *Ecology and Society* 14 (1): 44.

Ewing, K., 1996. Tolerance of four wetland plant species to flooding and sediment deposition. Environ. Exp. Bot. 36, 131–146.

Farjood, A., B. Melville, and A. Shamseldin. 2015. The Effect of Different Baffles on Hydraulic Performance of a Sediment Retention Pond. *Ecological Engineering,* 81: 228–32. doi:10.1016/j.ecoleng.2015.04.063.

Fogler, H. S. 1992. *Elements of Chemical Reaction Engineering*. Prentice-Hall, Englewood Cliffs, N.J..

Garcia, M.; Rhoads, B. (Eds.) *River, Coastal and Estuarine Morphodynamics*, 2005, p. 229-236.

German, J., and H. Kant. 1998. FEM-analys av strmningsförhållanden i en dagvattendamm (FEM-analysis of the hydraulic conditions in a stormwater detention pond). Vatten 54 (3): 183–90 (in Swedish).

Ghermandi, A., and E. Fichtman. 2015. Cultural Ecosystem Services of Multifunctional Constructed Treatment Wetlands and Waste Stabilization Ponds: Time to Enter the Mainstream? Ecological Engineering, 84: 615–23. doi:10.1016/j.ecoleng.2015.09.067.

Golzar, M. A brief review of pond residence times studies. In: *The Annual Postgraduate Research Student Conference,* Sheffield, UK: 2015, p. 32-37.

Gómez-Baggethun, E., Å. Gren, D. Barton, J. Langemeyer, T. McPhearson, P. O'Farrell, E. Andersson, Z. Hamstead, and P. Kremer. 2013. Urban Ecosystem Services. In Urbanization, Biodiversity and Ecosystem Services: Challenges and Opportunities, edited by T. Elmqvist, M. Fragkias, J. Goodness, et al., 175–251. Springer Netherlands. doi:10.1007/978-94-007-7088-1_11.

Green, J.C. Effect of macrophyte spatial variability on channel resistance. *Advances in Water Resources*, v. 29, n. 3, 2006, p. 426-438.

Greenway, M., C. Polson. 2007. Macrophyte establishment in stormwater wetlands: coping with flash flooding and fluctuating water levels in the subtropics. In: Proceedings from World Water and Environmental Congress, Tampa, Florida.

Gualtieri, C., Angeloudis, A., Bombardelli, F., Jha, S., Stoesser, T., 2017. On the Values for the Turbulent Schmidt Number in Environmental Flows. Fluids 2 (2), 17.

Headley, T., and C. Tanner. 2006. Application of Floating Wetlands for Enhanced Stormwater Treatment: A Review. NIWA Client Report, Auckland Regional Council, New Zealand.

Headley, T., and C. Tanner. 2012. Constructed wetlands with floating emergent macrophytes: an innovative stormwater treatment technology. *Crit. Rev. Environ. Sci. Technol*. 42, 2261e2310.

Hoeger, S. 1988. Schwimmkampen: Germany's artificial floating islands. *J. Soil Water Conserv*, 43, 304–306.
https://ofmpub.epa.gov/waters10/attains_nation_cy.control#prob_source.Infrastructure. *Ecological Engineering,* 58: 44–51.

Kadlec, R., and S. Wallace. 2009. Treatment Wetlands. 2nd ed. CRC Press, Boca Raton, FL.

Kearney, M., S. Fickbohm, and W. Zhu. 2013. Loss of Plant Biodiversity Over a Seven-Year Period in Two Constructed Wetlands in Central New York. *Environmental Management* 51 (5): 1067.

Khan, S., and A. Shamseldin. 2013. Design of Storm-Water Retention Ponds with Floating Treatment Wetlands. *J. of Environmental Engineering* 139 (11): 1343–49.

Khan, S., B. Melville, and A. Shamseldin. 2011. Retrofitting a Stormwater Retention Pond Using a Deflector Island. *Water Science & Technology* 63 (12): 2867–72.

Khan, S., B. Melville, and A. Shamseldin. 2013. Design of storm-water retention ponds with floating treatment wetlands. *J.Environmental Engineering*, *139*(11):1343-1349.

Kleeberg, A.; Köhler, J.; Sukhodolova, T.; Sukhodolov, A. Effects of aquatic macrophytes on organic matter deposition, resuspension and phosphorus entrainment in a lowland river. *Freshwater Biology*, v. 55, 2010, p. 326-345.

Knight, R., R. Clarke, and R. Bastian. 2001. Surface flow (SF) treatment wetlands as a habitat for wildlife and humans. *Water Science and Technology*, 44:27–37.

Kondziolka, J.M.; Nepf, H.M. Vegetation wakes and wake interaction shaping aquatic landscape evolution. *Limnology and Oceanography – Fluids & Environments*, v. 4, 2014, p. 106-119.

Krebs, C. 2009. *Ecology: The Experimental Analysis of Distribution and Abundance*. Pearson Benjamin Cummings, San Francisco, CA.

Krzikalla, F., 2005. Numerical investigation of the interaction between wind and forest and heterogeneous conditions. Master's Thesis, University of Karlsruhe.

Lane, S., D. Sample, A. Lazur, R. Winston, C. Streb, D. Ferrier, L. Linker and K. Brittingham, 2016, Recommendations of the Expert Panel to Define Removal Rates for Floating Treatment Wetlands in Existing Wet Ponds, Chesapeake Research Consortium, http://chesapeakestormwater.net/bmp-resources/floating-treatment-wetlands/

Larsen, L.G.; Harvey, J.W. Modeling of hydroecological feedbacks predicts distinct classes of landscape pattern, process, and restoration potential in shallow aquatic ecosystems. *Geomorphology*, v. 126, 2011, p. 279-296.

Lee, J., and M.-H. Li. 2009. The impact of detention basin design on residential property value: case studies using GIS in the hedonic price modeling. *Landscape and Urban Planning*, 89:7–16.

Lightbody, A., H. Nepf, and J. Bays. 2007. Mixing in deep zones within constructed treatment wetlands, *Ecological Engineering*, 29(2):209-220, doi:10.1016/j.ecoleng.2006.11.001.

Lightbody, A., M. Avener, and H. Nepf. 2008. Observations of short-circuiting flow paths within a constructed treatment wetland in Augusta, Georgia, USA. *Limnol. Ocean.*, 53(3):1040- 1053.

Lovell, S., and D. Johnston. 2009. Designing Landscapes for Performance Based on Emerging Principles in Landscape Ecology. *Ecology and Society* 14 (1): 44.

Machado Xavier, M. L., Janzen, J. G. and Nepf, H., 2017. Numerical modeling study to compare the nutrient removal potential of different floating treatment island configurations in a stormwater pond. *Ecological Engineering* 111, 78-84

Marjoribanks, T.I.; Hardy, R.J.; Lane, S.N.; Parsons, D.R. High-resolution numerical modelling of flow-vegetation interactions. *Journal of Hydraulic Research*, v. 52, n. 6, 2014, p. 775-793.

Melbourne Water. 2002. *Constructed wetland systems: Design guidelines for developers*. Melbourne, Australia: Melbourne Water.

Menter, F. R., Kuntz, M., and Langtry, R. 2003. Ten years of industrial experience with the SST turbulence model. *Turbulence, heat and mass transfer*, *4*(1), 625-632.

Moore, T. and W. Hunt. 2012. Ecosystem Service Provision by Stormwater Wetlands and Ponds – A Means for Evaluation? *Water Research*, Special Issue on Stormwater in Urban Areas, 46 (20): 6811–23.

Moore, T. and W. Hunt. 2013. Predicting the Carbon Footprint of Urban Stormwater Nepf, H.M. Drag, turbulence, and diffusion in flow through emergent vegetation. *Water Resources Research*, v. 35, n. 2, 1999, p. 479-489.

Nepf, H.M. Hydrodynamics of vegetated channels. *Journal of Hydraulic Research*, v. 50, n. 3, 2012, p. 262-279.

Patrick Ambrosio, “President Proposes Cut To EPA Funding for Fiscal Year 2015,” *Bloomberg*, March 6, 2014, http://www.bloomberg.com/news/2014-03-06/president-proposes-cut-to-epa-funding-for-fiscal-year-2015.html; OCFO US EPA, “FY 2015 Budget,” Overviews and Factsheets, accessed January 25, 2015, http://www2.epa.gov/planandbudget/fy2015; Ronald White, “Congress Slashes EPA Budget Again Despite Strong Public Support for Strengthening Health Protections | Center for Effective Government,” accessed January 25, 2015,

http://www.foreffectivegov.org/blog/congress-slashes-epa-budget-again-despite-strong-public-support-strengthening-health-protection.

Pavlineri N., N. Skoulikidis, A. Vassilios, A. Tsihrintzis. 2017. Constructed Floating Wetlands: A review of research, design, operation and management aspects, and data meta-analysis. Chemical Engineering Journal 308: 1120–1132

Persson, J. 2000. The Hydraulic Performance of Ponds of Various Layouts. Urban Water 2 (3): 243–50, doi:10.1016/S1462-0758(00)00059-5.

Persson, J., N. Somes, and T. Wong. 1999. Hydraulics Efficiency of Constructed Wetlands and Ponds. *Water Science and Technology* 40 (3): 291–300. doi:10.1016/S0273- 1223(99)00448-5.

Rominger, J.T., Nepf, H.M., 2011. Flow adjustment and interior flow associated with a rectangular porous obstruction. *Journal of Fluid Mechanics* 680, p. 636–659.

Rousseau, D., E. Lesage, A. Story, P.A. Vanrolleghem, and N. De Pauw. 2008. Constructed Wetlands for Water Reclamation. Desalination 218 (1–3): 181–89. doi:10.1016/j.desal.2006.09.034.

Savickis, J., A. Bottacin-Busolin, M. Zaramella, N. Sabokrouhiyeh, and A. Marion. 2016. Effect of a Meandering Channel on Wetland Performance. J. Hydrology 535: 204–10, doi:10.1016/j.jhydrol.2016.01.082.

Shannon, C., and W. Weaver. 1949. *The Mathematical Theory of Communication.* University of Illinois Press, Urbana, IL.

Shilton, A. 2001. Studies into the Hydraulics of Waste Stabilisation P 725 onds. Ph.D. Dissertation, Turitea Campus, Palmerston North, New Zealand: Massey University.
Sleeper, B., and R. Ficklin. 2016. Edaphic and Vegetative Responses to Forested Wetland Restoration with Created Microtopography in Arkansas. Ecological Restoration, 34 (2): 117–23.

Sleeper, B., and R. Ficklin. 2016. Edaphic and Vegetative Responses to Forested Wetland Restoration with Created Microtopography in Arkansas. *Ecological Restoration*, 34 (2): 117–23.

Smith, M., and M. Kalin, 2000. Floating wetland vegetation covers for suspended solids removal. Proceedings of the Quebec 2000: Millennium Wetland Event. Quebec City, Quebec: 244.

Snøhetta. 2017. MAX IV Laboratory Landscape. http://snohetta.com/projects/70-max-iv732 laboratory-landscape

Sonnenwald, F.; Guymer, I.; Stovin, V. Computational fluid dynamics modelling of residence times in vegetated stormwater ponds. *Water Management*, v. 171, n. 2, 2017, p. 1-11.

Stamou, A., 2002. Verification and application of a mathematical model for the assessment of the effect of guiding walls on the hydraulic efficiency of chlorination tanks. *J. Hydroinformatics*, *4*(4):245-254.

Stoesser, T.; Kim, S.J.; Diplas, P. Turbulent flow through idealized emergente vegetation. *Journal of Hydraulic Engineering*, v. 136, n. 12, 2010, p. 1003-1017.

Stoesser, T.; Salvador, G.P.; Rodi, W.; Diplas, P. Large Eddy Simulation of turbulent flow through submerged vegetation. *Transport in Porous Media*, v. 78, 2009, p. 347-365.

Sukhodolov, A.; Sukhodolova, T. Morphodynamics and hydraulics of vegetated river reaches: a case study on the Müggelspree in Germany. In: Parker, G.;
Tal, M.; Paola, C. Dynamic single-thread channels maintained by the interaction of flow and vegetation. *Geomorphology*, v. 35, n. 4, 2007, p. 347-350.

Tanner, C., and T. Headley. 2011. Components of floating emergent macrophyte treatment wetlands influencing removal of stormwater pollutants. *Ecological Engineering*, *37*(3):474-486.

Taylor, J.R. 1997. An Introduction to Error Analysis: The study of uncertainties in physical experiments. 2nd Ed. University Science Books. ISBN-13: 978-0-935702-75-0
Technical Assistance Projects. https://www.epa.gov/sites/production/files/2016-01/documents/gi_tech_asst_summary_508final010515_3.pdf.

Temmerman, S.; Bouma, T.J.; Van De Koppel, J.; Van Der Wal, D.; De Vries, M.B.; Herman, P.M.J. Vegetation causes channel erosion in a tidal landscape. *Geology*, v. 35, n. 7, 2007, p. 631-634.

Thackston, E., F. D. Shields, and P. Schroeder. 1987. Residence Time Distributions of Shallow Basins. *J. Environmental Engineering*, 113 (6): 1319–32. U.S. EPA. 2000. Guiding Principles for Constructed Treatment Wetlands: Providing for Water Quality and Wildlife Habitat. EPA 843-B-00-003. Washington, D.C.

Tsavdaris, A.; Mitchell, S.; Williams, J. Use of CFD to model emergent vegetation in detention ponds. *Journal of Engineering and Applied Sciences*, v. 8, n. 7, 2013, p. 495-503.

U.S. EPA. 2000. Guiding Principles for Constructed Treatment Wetlands: Providing for Water Quality and Wildlife Habitat. EPA 843-B-00-003. Washington, D.C.
https://nepis.epa.gov/Exe/ZyPDF.cgi/2000536S.PDF?Dockey=2000536S.PDF.

U.S. EPA. 2015. Tools, Strategies and Lessons Learned from EPA Green InfrastructureTechnical Assistance Projects.
https://www.epa.gov/sites/production/files/2016-01/documents/gi_tech_asst_summary_508final010515_3.pdf.

U.S. EPA. 2015. Tools, Strategies and Lessons Learned from EPA Green Infrastructure

U.S. EPA. 2017. “National Summary of State Information.” *Water Quality Assessment and TMDL Information*. Accessed May 5.

Vandenbruwaene, W.; Temmerman, S.; Bouma, T.J.; Klaassen, P.C.; De Vries, M.B.; Callaghan, D.P.; Van Steeg, P.; Dekker, F.; Van Duren, L.A.; Martini, E.; Balke, T.; Biermans, G.; Schoelynck, J.; Meire, P. Flow interaction with dynamic vegetation patches: Implications for biogeomorphic evolution of a tidal landscape. *Journal of*

Geophysical Research, v. 116, F01008, 2011.

Vivian-Smith, G. 1997. Microtopographic Heterogeneity and Floristic Diversity in Experimental Wetland Communities. J. Ecology 85 (1): 71–82.

Walsh, J. 2014. Chapter 2: Our Changing Climate. In *Climate Change Impacts in the United States: The Third National Climate Assessment*, edited by J.M. Melillo, T. Richmond, and G.W. Yohe, 19–67. U.S. Global Change Research Program.

Werner T., R. Kadlec. 1996. Application of residence time distributions to stormwater treatment systems. *Ecological Engineering*, 7(3): 213-234.

White, B.; Nepf, H.M. Scalar transport in random cylinder arrays at moderate Reynolds number. *Journal of Fluid Mechanics*, v. 487, 2003, p. 43-79.

White, S. and, M. Cousins. 2013. Floating treatment wetland aided remediation of nitrogen and phosphorus from simulated stormwater runoff. *Ecological Engineering*, *61*, 207-215.

Wildlife Conservation. In Proceedings of the Eighth International Conference on Wetland Systems for Water Pollution Control, 2: 1024–37.

Wilson, C.A.M.E.; Stoesser, T.; Bates, P.D. Modelling of open channel flow through vegetation. In: Bates, P.D.; Lane, S.N.; Ferguson, R.I. (Eds.) *Computational Fluid Dynamics: Applications in Environmental Hydraulics*. John Wiley & Sons Ltd, Inglaterra, 2005, p. 395-428.

Winston, R., W. Hunt, S. Kennedy, L. Merriman, J. Chandler, and D. Brown, 2013. Evaluation of floating treatment wetlands as retrofits to existing stormwater retention ponds. *Ecological Engineering*, 54: 254-265, http://linkinghub.elsevier.com/retrieve/pii/S0925857413000384.

Wolf, K., C. Ahn, and G. Noe. 2011. Microtopography Enhances Nitrogen Cycling and Removal in Created Mitigation Wetlands. *Ecological Engineering*, 37: 1398–1406.

Worrall, P., K. Peberdy, and M. Millett. 1997. Constructed Wetlands and Nature Conservation. Water Science & Technology, 35 (5): 205–13. doi:10.1016/S0273-1223(97)00070-X.

Wurth, A. 1996. Why Aren't All Engineers Ecologists? In *Engineering Within Ecological Constraints*, edited by P. Schulze, pp.129–40. Washington, D.C.: National Academies Press. http://www.nap.edu/catalog/4919.

Yamasaki, T.N.; Janzen, J.G.; De Lima, P.H.S. Representando a vegetação na modelagem computacional de *wetlands*. In: *Anais do 3º Simpósio Brasileiro Sobre Wetlands Construídos*. Campo Grande: UCDB, 2017, p. 303-311.

Zong, L.; Nepf, H.M. Vortex development behind a finite porous obstruction in a channel. *Journal of Fluid Mechanics*, v. 691, 2012, p. 368-391.